INTERNATIONAL JOURNAL FOR NUMERICAL METHODS IN FLUIDS
Int. J. Numer. Meth. Fluids (2012)
Published online in Wiley Online Library (wileyonlinelibrary.com/journal/nmf). DOI: 10.1002/fld.3740

Discrete filter operators for large-eddy simulation using high-order spectral difference methods

Guido Lodato[1,2,*,†], Patrice Castonguay[1] and Antony Jameson[1]

[1]*Department of Aeronautics and Astronautics, Stanford University, Stanford, CA, USA*
[2]*Center for Turbulence Research, Stanford University, Stanford, CA, USA*

SUMMARY

The combination of a high-order unstructured spectral difference (SD) spatial discretization scheme with sub-grid scale (SGS) modeling for large-eddy simulation is investigated with particular focus on the consistent implementation of a structural mixed model based on the scale similarity hypothesis. The difficult task of deriving a consistent formulation for the discrete filter within the SD element of arbitrary order led to the development of a new class of three-dimensional constrained discrete filters. The discrete filters satisfy a set of selected criteria and are completely local within the SD element. Their weights can be automatically computed at run time from the number of solution points within each element and the expected filter cutoff length scale. The novel discrete filters can be applied to any SGS model involving explicit filtering and to a broad class of high-order discontinuous finite element numerical schemes. The code is applied to the computation of turbulent channel flows at three Reynolds numbers, namely $\mathrm{Re}_\tau = 180$, 395, and 590 (based on the friction velocity u_τ and channel half-width δ). Results from computations with and without the SGS model are compared against results from direct numerical simulation. The numerical experiments suggest that the results are sensitive to the use of the SGS model, even when a high-order numerical scheme is used, especially when the grid resolution is kept relatively low and mostly in terms of resolved Reynolds stresses. Results obtained using existing filters based on the projection of the solution over lower-order polynomial bases are also shown and demonstrate that these filters are inadequate for SGS modeling purposes, mostly because of their inability to enforce the selected cutoff length scale with sufficient accuracy. The use of the similarity mixed formulation proved to be particularly accurate in reproducing SGS interactions, confirming that its well-known potential can be realized in conjunction with state-of-the-art high-order numerical schemes. Copyright © 2012 John Wiley & Sons, Ltd.

Received 30 March 2012; Revised 2 August 2012; Accepted 21 September 2012

KEY WORDS: high-order methods; LES; turbulence models; discrete filters; spectral difference; channel flow

1. INTRODUCTION

Because of the continuous and growing development of available computational resources during the last decade, there has been an increased interest in the use of large-eddy simulation (LES) for simulating engineering flows of practical interest. Many engineering applications—for example, those involving vortex-dominated flow dynamics, transitional or massively detached flows, turbulent mixing and combustion, or aerodynamic noise—require the numerical simulation of flows over complex geometries with a level of detail that the most widely used Reynolds averaged Navier–Stokes (RANS) simulations cannot fulfill. For such applications, LES represents the most efficient approach.

Notwithstanding the considerable effort that has been devoted to the development of accurate and relatively reliable sub-grid scale (SGS) models for LES, in most cases, the underlying

*Correspondence to: Guido Lodato, Department of Aeronautics and Astronautics, Stanford University, Stanford, CA, USA.
†E-mail: glodato@stanford.edu

numerical methods available within the framework of industrial CFD applications rely upon highly dissipative schemes. The inherent numerical dissipation introduced by such numerical schemes limits their ability to correctly represent the high frequency range of the spectrum of turbulence.

On the other hand, caution should be exercised when using less dissipative high-order numerical methods to perform implicit LES without any SGS model, namely compute a truncated turbulent spectrum designating whatever amount of numerical dissipation method brought by the numerical scheme to set small-scale dissipation. Depending on the problem under study and the grid resolution used in the computation, it is uncertain whether such an approach would produce accurate and useful results. In fact, numerical dissipation can supposedly handle dissipative processes, which are confined to small scales, but can certainly not reproduce complex interactions between large and small scales, which are often observed in LES.

Hence, it is necessary to combine high-order numerical schemes with advanced SGS modeling techniques for LES to become a valuable and reliable tool for fundamental flow physics and industrial applications. Unfortunately, most of the available high-order numerical schemes are designed to be used on Cartesian or very smooth structured curvilinear meshes [1–5], and therefore, they are inadequate to simulate turbulent flows over complex geometries. In the current work, a high-order unstructured solver is combined with an explicit filtering LES method, thus allowing highly accurate turbulent flow computations on realistic geometries that were previously possible with low-order schemes only.

High-order numerical schemes for solving the compressible Navier–Stokes equations on unstructured grids have been widely studied during the last decade. By far, the most mature and widely used of these schemes are based on the discontinuous Galerkin (DG) method [6, 7]. However, several alternative high-order methods have been recently proposed, including spectral difference (SD)-type schemes [8–15], which potentially offer increased efficiency compared with DG methods (as well as being simpler to implement). It has recently been demonstrated [16–18] that, for the case of one-dimensional (1D) linear advection, both SD-type and nodal DG-type schemes can be formulated within a unifying flux reconstruction (FR) framework [9]. Such a unifying framework is efficient, is straightforward to implement, and allows direct comparisons to be made between various SD and DG methods. The extension of the FR methodology to a variety of element shapes and the consistent inclusion of viscous terms have also been recently addressed [19–21].

In the present work, a compressible solver for three-dimensional unstructured hexahedral grids based on the SD scheme is adopted. The scheme from the energy-stable FR formalism by setting the relevant stability constant accordingly (see Vincent *et al.* [17] and Section 3.5.2 therein for details). In this respect, the SD scheme is taken as a representative of the broader class of FR and DG methods. The SD method has been successfully applied to viscous compressible flows with shocks [22], implicit LES of turbulent channel flow [23], and flow around circular cylinders [24–26], as well as transitional flows over an SD7003 airfoil [27]. The combination of the SD method with SGS modeling techniques for explicit LES, on the other hand, has not been widely studied. Parsani *et al.* [28] obtained encouraging results using the wall-adapting local eddy viscosity (WALE) [29] model, but their analysis was restricted to two-dimensional flows. A three-dimensional computation of turbulent flow in a muffler at $\mathrm{Re} = 46{,}650$ was also reported [30]. In this study, focus is given to the more challenging implementation of a *structural* SGS model based on the scale similarity assumption [31, 32], namely the WALE Similarity Mixed model, hereafter indicated as the WSM model, proposed by Lodato *et al.* [33]. Note that, compared with *functional* models such as those based on the eddy viscosity assumption, which are designed to reproduce the effects of SGS terms on the resolved flow field by means of the divergence of the SGS tensor, structural models are designed to reproduce the structure of the SGS stress tensor itself and hence can generally attain relatively high levels of correlation at tensor level [34, 35].

The development of efficient approaches to filter the solution obtained from high-order finite element numerical schemes, such as the SD method used here, is not straightforward. The peculiar distribution of points within the element and the requirement of *locality* of the numerical filter operator therein lead inevitably to asymmetric filtering operators acting on non-uniform points. In this scenario, designing operators with sufficiently controlled properties turns out to be extremely difficult, especially when the desired cutoff length scale is smaller than twice the element resolution

DOI: 10.1002/fld

(as would be the case for a dynamic modeling approach). Existing techniques that involve projection on polynomial bases of lower order or sharp cutoff in modal space [22,36,37] do not allow any direct control on the cutoff length scale which, as will be shown in Section 2.3, can result significantly overestimated. Their applicability is hence limited to dynamic models, which adopt wider filters and where the necessary averaging procedures can supposedly mitigate the numerical deficiencies of the filtering operators. In cases where the cutoff length of the filter needs to be accurately prescribed, more suitable filtering strategies has to be developed, as reported in this work.

To the authors' knowledge, the present work represents the first implementation of a structural SGS model in a three-dimensional solver that uses the SD method. Moreover, the proposed implementation of constrained discrete filters of arbitrary order is suitable for any kind of high-order discontinuous finite element method that uses elements that allow tensor product (e.g., hexahedral elements) including the FR and nodal DG methods.

2. MATHEMATICAL FORMULATION

2.1. The numerical scheme

In the present work, the Navier–Stokes equations are solved using the high-order unstructured SD spatial discretization. The formulation of the equations on hexahedral grids is similar to the formulation by Sun *et al.* [13], which is here summarized for completeness. The unsteady compressible Navier–Stokes equations in conservative form are written as

$$\frac{\partial \boldsymbol{U}}{\partial t} + \frac{\partial \boldsymbol{F}^k}{\partial x_k} = \boldsymbol{0}, \tag{1}$$

where $\boldsymbol{U} = \begin{pmatrix} \rho & \rho u_1 & \rho u_2 & \rho u_3 & \rho e \end{pmatrix}^{\mathrm{T}}$ is the vector of conservative variables and $\boldsymbol{F}^k = \boldsymbol{F_I}^k - \boldsymbol{D}^k$ accounts for the inviscid and viscous flux vectors, which are defined as

$$\boldsymbol{F_I}^k = \begin{pmatrix} \rho u_k \\ \rho u_1 u_k + \delta_{1k} p \\ \rho u_2 u_k + \delta_{2k} p \\ \rho u_3 u_k + \delta_{3k} p \\ (\rho e + p) u_k \end{pmatrix} \quad \text{and} \quad \boldsymbol{D}^k = \begin{pmatrix} 0 \\ 2\mu A_{1k} \\ 2\mu A_{2k} \\ 2\mu A_{3k} \\ 2\mu u_j A_{kj} + \frac{\mu c_{\mathrm{p}}}{\mathrm{Pr}} \frac{\partial T}{\partial x_k} \end{pmatrix}. \tag{2}$$

In the preceding equations, ρ is the fluid's density, u_k is the velocity vector, e is the total energy (internal + kinetic), μ is the dynamic viscosity, A_{ij} is the deviatoric part of the deformation tensor, c_{p} is the specific heat capacity at constant pressure, and Pr is the Prandtl number.

For an efficient implementation to be achieved, all elements in the physical domain are transformed to a standard cubic element described by local coordinates $\boldsymbol{\xi} = (\xi_1, \xi_2, \xi_3)$, with $\boldsymbol{\xi} \in [0:1]^3$. The relevant transformation can be written as

$$x_i(\boldsymbol{\xi}) = \sum_{j=1}^{N_{\mathrm{p}}} M_j(\boldsymbol{\xi}) x_i^j, \quad (i = 1, 2, 3), \tag{3}$$

where N_{p} is the number of points used to define the physical elements, x_i^j are the Cartesian coordinates at those points, and $M_j(\boldsymbol{\xi})$ are the shape functions. The governing equations in the physical domain are then transferred into the computational domain, where they take the form

$$\frac{\partial \boldsymbol{\mathcal{U}}}{\partial t} + \frac{\partial \boldsymbol{\mathcal{F}}^k}{\partial \xi_k} = \boldsymbol{0}, \tag{4}$$

in which

$$\boldsymbol{\mathcal{U}} = |\det(\boldsymbol{J})| \boldsymbol{U} \quad \text{and} \quad \boldsymbol{\mathcal{F}}^k = |\det(\boldsymbol{J})| \frac{\partial \xi_k}{\partial x_j} \boldsymbol{F}^j \tag{5}$$

and $\det(\boldsymbol{J})$ represents the determinant of the Jacobian matrix $\boldsymbol{J}_{ij} = \partial x_i / \partial \xi_j$.

DOI: 10.1002/fld

Within each standard element, two sets of points are defined, namely the solution points and the flux points, as schematically illustrated in Figure 1 for a two-dimensional element. For a degree $(N-1)$ polynomial to be constructed in each coordinate direction, solutions at N points are required. Note that, in a recent work, Jameson [16] utilized an FR formulation [9] to prove that the SD method is linearly stable for all orders of accuracy, provided that the interior flux points are placed at the Gauss–Legendre quadrature points. Moreover, for the non-linear case, the choice of locating the solution points at the Gauss–Legendre quadrature points is optimal in reducing aliasing errors and providing good conditioning [38]. Accordingly, the N solution points in 1D are chosen to be the Gauss–Legendre quadrature points, which are obtained as the roots of the equation

$$P_N(\zeta) = \frac{2N-1}{N}\zeta P_{N-1}(\zeta) - \frac{N-1}{N}P_{N-2}(\zeta) = 0, \tag{6}$$

where $P_N(\zeta)$ is the Legendre polynomial of order N, $P_0(\zeta) = 1$, $P_1(\zeta) = \zeta$, and $\zeta = 2\xi - 1$.

The flux points are selected to be the Gauss–Legendre quadrature points of order $N-1$ plus the two end points 0 and 1. The fluxes at the interior points are calculated from the interpolated states defined by the solution polynomial, whereas the flux at each endpoint is calculated as a common interface flux depending on the left and right values at the interface. Using the solutions at N solution points, a degree $(N-1)$ polynomial can be built is obtained using the following Lagrange basis defined as

$$h_i(\xi) = \prod_{s=1, s\neq i}^{N} \left(\frac{\xi - \xi_s}{\xi_i - \xi_s}\right). \tag{7}$$

Similarly, using the fluxes at $(N+1)$ flux points, a degree N polynomial is obtained for the flux using the Lagrange basis

$$l_{i+1/2}(\xi) = \prod_{s=0, s\neq i}^{N} \left(\frac{\xi - \xi_{s+1/2}}{\xi_{i+1/2} - \xi_{s+1/2}}\right). \tag{8}$$

The reconstructed solution for the conserved variables in the standard element is then obtained as the tensor product of the three 1D polynomials,

$$\boldsymbol{U}(\boldsymbol{\xi}) = \sum_{k=1}^{N}\sum_{j=1}^{N}\sum_{i=1}^{N} \frac{\mathcal{U}_{i,j,k}}{|J_{i,j,k}|} h_i(\xi_1) h_j(\xi_2) h_k(\xi_3), \tag{9}$$

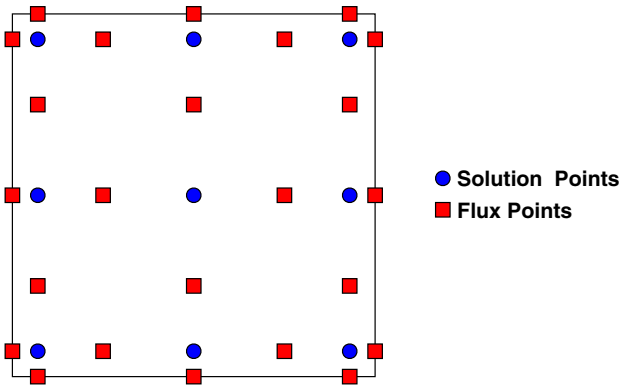

Figure 1. Position of solution (circles) and flux (squares) points on the standard third-order two-dimensional spectral difference element.

DOI: 10.1002/fld

where i, j, and k are the indices of the solution points within each standard element. Similarly, the reconstructed flux polynomials take the following form:

$$\mathcal{F}^1(\boldsymbol{\xi}) = \sum_{k=1}^{N}\sum_{j=1}^{N}\sum_{i=0}^{N} \mathcal{F}^1_{i+1/2,j,k}\, l_{i+1/2}(\xi_1)\, h_j(\xi_2)\, h_k(\xi_3), \tag{10}$$

$$\mathcal{F}^2(\boldsymbol{\xi}) = \sum_{k=1}^{N}\sum_{j=0}^{N}\sum_{i=1}^{N} \mathcal{F}^2_{i,j+1/2,k}\, h_i(\xi_1)\, l_{j+1/2}(\xi_2)\, h_k(\xi_3), \tag{11}$$

$$\mathcal{F}^3(\boldsymbol{\xi}) = \sum_{k=0}^{N}\sum_{j=1}^{N}\sum_{i=1}^{N} \mathcal{F}^3_{i,j,k+1/2}\, h_i(\xi_1)\, h_j(\xi_2)\, l_{k+1/2}(\xi_3). \tag{12}$$

A Riemann solver is employed to compute the common inviscid flux at each cell interface to ensure both conservation and stability. In the current implementation, the Roe solver [39] with entropy fix [40] was used. The left and right states represent here the solution on both sides of the shared edge flux point. The viscous flux is a function of both the conserved variables and their gradients; therefore, the solution gradients have to be calculated at the flux points. The average approach described by Sun *et al.* [13] is used to compute the viscous fluxes at the cell interfaces. Time integration is performed using a third-order total variation diminishing Runge–Kutta scheme [41, 42].

2.2. LES modeling approach

Within the framework of LES, large scales are directly resolved, whereas small scales (of the order of a cutoff length Δ_g or less) are not. Such a length scale separation is achieved in physical space by means of the low-pass filter operation at Δ_g. The filtering operation can be explicitly performed on the numerical solution obtained on a relatively fine mesh, or as is common practice, the computational grid is supposed to inherently perform the filtering operation, such that the results obtained from the computation may be regarded as being representative of filtered quantities, the cutoff length scale being related to the local grid resolution.

The latter approach is adopted in the present study. Therefore, what is solved for are the filtered Navier–Stokes equations, which are formally obtained from Equation (1) after applying the *bar* filter operator and the density-weighted Favre filter operator *tilde*, such that the identity $\overline{\rho\varphi} = \overline{\rho}\tilde{\varphi}$ holds true:

$$\frac{\partial \overline{\boldsymbol{U}}}{\partial t} + \frac{\partial \overline{\boldsymbol{F_I}}^k}{\partial x_k} = \frac{\partial \overline{\boldsymbol{D}}^k}{\partial x_k}, \tag{13}$$

with $\overline{\boldsymbol{U}} = \left(\begin{array}{cccccc} \overline{\rho} & \overline{\rho u_1} & \overline{\rho u_2} & \overline{\rho u_3} & \overline{\rho e} \end{array}\right)^{\mathrm{T}}$,

$$\overline{\boldsymbol{F_I}}^k = \begin{pmatrix} \overline{\rho u}_k \\ \overline{\rho u}_1 \tilde{u}_k + \delta_{1k}\overline{\varpi} \\ \overline{\rho u}_2 \tilde{u}_k + \delta_{2k}\overline{\varpi} \\ \overline{\rho u}_3 \tilde{u}_k + \delta_{3k}\overline{\varpi} \\ (\overline{\rho e} + \overline{\varpi})\tilde{u}_k \end{pmatrix}, \quad \overline{\boldsymbol{D}}^k = \begin{pmatrix} 0 \\ 2\overline{\mu}\tilde{A}_{1k} + \tau^{\mathrm{d}}_{1k} \\ 2\overline{\mu}\tilde{A}_{2k} + \tau^{\mathrm{d}}_{2k} \\ 2\overline{\mu}\tilde{A}_{3k} + \tau^{\mathrm{d}}_{3k} \\ 2\overline{\mu}\tilde{u}_j\tilde{A}_{kj} + \frac{\overline{\mu}c_{\mathrm{p}}}{\mathrm{Pr}}\frac{\partial\tilde{\vartheta}}{\partial x_k} + q_k \end{pmatrix}, \tag{14}$$

where the superscript 'd' refers to the deviatoric part of the relevant tensor, namely $\tau^{\mathrm{d}}_{ij} = \tau_{ij} - (1/3)\delta_{ij}\tau_{kk}$. The tensor τ_{ij} and the vector q_k represent the usual unclosed SGS terms,

$$\tau_{ij} = \overline{\rho u}_i \tilde{u}_j - \overline{\rho u_i u_j}, \tag{15}$$

$$q_k = (\overline{\rho e} + \overline{\varpi})\tilde{u}_k - \overline{(\rho e + p)u_k} \simeq \gamma c_{\mathrm{v}}(\overline{\rho\vartheta}\,\tilde{u}_k - \overline{\rho T u_k}). \tag{16}$$

DOI: 10.1002/fld

In particular, $\overline{\varpi}$ and $\tilde{\vartheta}$ are the filtered *macro-pressure* and *macro-temperature*, respectively, which may include all [43, 44] or just a part [33] of the trace of the SGS stress tensor, these quantities being related by the usual equation of state, namely, $\overline{\varpi} = \overline{\rho} R \tilde{\vartheta}$ (cf. [33, 43, 44] for details about the underlying hypotheses).

In general, the SGS model has to be designed such that: (i) it is active only where the solution is under resolved by the grid, and in particular, it vanishes with the correct asymptotical behavior close to solid boundaries [45, 46]; (ii) it accurately represents the peculiar SGS interactions resulting from the use of non-Reynolds filtering operators, that is, operators that, as opposed to the ensemble or time averaging adopted in RANS, are not idempotent in spectral space [47]; and (iii) it is not too dissipative, hence leading to undesired relaminarization phenomena, and at the same time, it does not destabilize the flow field because of insufficient dissipation or incorrect representation of turbulent energy *backscatter* events.

In order for the three aforementioned requirements to be met, the present study focuses on a structural model based on the scale similarity assumption [31, 32, 34, 48]. Hence, the fundamental assumption is made that the statistical features of tensors constructed on the sub-grid scales are similar to those of analogous tensors computed on the basis of the smallest resolved scales. Similarity models, in particular, remove the hypothesis of alignment between the proper axes of the SGS stress tensor and those of the resolved shear stress tensor, which is inherent in the eddy viscosity assumption. In simulations that use similarity models, good correlation has been observed between the real and modeled SGS stresses. Good correlation was also observed between real and modeled local SGS energy flux, even in regions characterized by energy backscatter, thus suggesting that the Leonard tensor introduced by the scale similarity assumption can be used to predict complex SGS interactions such as those leading to energy backscatter [34, 49].

In the perspective of developing a similarity mixed formulation [48–55] with correct near-wall scaling without relying on dynamic procedures, a WALE formulation [29] for the eddy viscosity term was recently proposed by Lodato *et al.* [33]. The resulting WSM model limits the use of the explicit filtering operator to the computation of the modified Leonard tensor only. The relevant closures are computed as

$$\tau_{ij}^{\mathrm{d}} = 2\overline{\rho}\nu_{\mathrm{sgs}}\tilde{A}_{ij} - \overline{\rho}\left(\widehat{\tilde{u}_i\tilde{u}_j} - \widehat{\tilde{u}}_i\widehat{\tilde{u}}_j\right)^{\mathrm{d}}, \tag{17}$$

$$q_k = \gamma\overline{\rho}\kappa_{\mathrm{sgs}}\frac{\partial\widetilde{e_{\mathrm{I}}}}{\partial x_k} - \gamma\overline{\rho}\left(\widehat{\widetilde{e_{\mathrm{I}}}\tilde{u}_k} - \widehat{\widetilde{e_{\mathrm{I}}}}\widehat{\tilde{u}}_k\right), \tag{18}$$

where $\widetilde{e_{\mathrm{I}}}$ is the resolved internal energy and the *hat* operator represents filtering at cutoff length $\alpha\Delta_{\mathrm{g}}$, with $\alpha \geqslant 1$ and sufficient localization in physical space [34].

With regard to the eddy viscosity terms, the SGS kinematic viscosity, ν_{sgs}, and thermal diffusivity, κ_{sgs}, are computed as [29]

$$\nu_{\mathrm{sgs}} = C_{\mathrm{w}}^2\Delta_{\mathrm{g}}^2\frac{\left(\tilde{s}_{ij}^{\mathrm{d}}\tilde{s}_{ij}^{\mathrm{d}}\right)^{3/2}}{\left(\tilde{A}_{ij}\tilde{A}_{ij}\right)^{5/2} + \left(\tilde{s}_{ij}^{\mathrm{d}}\tilde{s}_{ij}^{\mathrm{d}}\right)^{5/4}} \quad \text{and} \quad \kappa_{\mathrm{sgs}} = \frac{\nu_{\mathrm{sgs}}}{\mathrm{Pr}_{\mathrm{sgs}}}, \tag{19}$$

where C_{w} is the model constant, $\tilde{s}_{ij}^{\mathrm{d}}$ is the traceless symmetric part of the square of the resolved velocity gradient tensor $\tilde{g}_{ij} = \partial\tilde{u}_i/\partial x_j$, namely $\tilde{s}_{ij}^{\mathrm{d}} = (1/2)\left(\tilde{g}_{ij}^2 + \tilde{g}_{ji}^2\right) - (1/3)\delta_{ij}\tilde{g}_{kk}^2$ with $\tilde{g}_{ij}^2 = \tilde{g}_{ik}\tilde{g}_{kj}$, and Δ_{g} is a measure of the grid cutoff length scale. In particular, assuming that the actual resolution of the SD element in computational space is equal to $\Delta = 1/N$, the cutoff length Δ_{g} can be evaluated following the same procedure suggested by Parsani *et al.* [28], namely

$$\Delta_{\mathrm{g}}(\boldsymbol{\xi}) \sim \left[\frac{|\det(\boldsymbol{J}(\boldsymbol{\xi}))|}{N^3}\right]^{1/3} = \Delta|\det(\boldsymbol{J}(\boldsymbol{\xi}))|^{1/3}. \tag{20}$$

DOI: 10.1002/fld

In line with what had been pointed out by Nicoud and Ducros [29], the model constant C_w was found to show some grid dependency. In the present study, C_w was set to 0.3, a value that was also used by Temmerman *et al.* [56] and that was found to be optimal, whereas the SGS Prandtl number, Pr_{sgs}, was assumed constant and equal to 0.5 [53, 55]. With regard to wall scaling, it is readily verified [57] that the asymptotic behavior of the SGS stress computed from Equation (17) is correctly predicted as

$$\langle \tau_{11}^{wsm} \rangle \sim x_2^2, \quad \langle \tau_{22}^{wsm} \rangle \sim x_2^2, \quad \langle \tau_{33}^{wsm} \rangle \sim x_2^2, \tag{21}$$

$$\langle \tau_{12}^{wsm} \rangle \sim x_2^3, \quad \langle \tau_{13}^{wsm} \rangle \sim x_2^2, \quad \langle \tau_{23}^{wsm} \rangle \sim x_2^3, \tag{22}$$

where the preceding relations refer to the deviator of the modeled sub-grid stress when the wall is orthogonal to x_2. As a final remark, it is worth noting that the WSM model can be easily reduced to the standard WALE formulation by simply switching off the computation of the modified Leonard terms in Equations (17) and (18).

2.3. Constrained discrete filters for the spectral difference method

When similarity mixed SGS models are used, such as the WSM model used in this study, explicit filtering represents a key ingredient to approximate SGS interactions. This is carried out by assuming similarity within a narrow band of frequencies in the vicinity of the cutoff frequency characteristic of the mesh. As mentioned in Section 2.2, similarity is assumed between the sub-grid scales and the smallest resolved scales, whose contribution is evaluated as the difference between the filtered and twice-filtered fields. Hence, the explicit filter should be designed to have sufficient localization in physical space and to ensure a certain selected cutoff length scale. For instance, the box filter in physical space is generally used because of its locality and ease of implementation [33, 52]. Lodato *et al.* [33], in particular, used a discrete approximation with cutoff length scale $\Delta_c = 4/3\Delta_g$ according to what was proposed by Akhavan *et al.* [48], this filter width being an optimal size to sufficiently isolate the smallest resolved scales. In the present study, Δ_c is fixed at $1.5\Delta_g$, a value that is still small enough to achieve the desired small-scale selection.

To develop a mixed similarity formulation to be applied with the SD method, the above ideas have to be generalized in a way that is numerically consistent with the use of SD elements. In particular, because the SGS model terms are evaluated at the flux points, the filtered field needs to be evaluated at the same flux points starting from the discrete solution at the solution points. This can be achieved by filtering the solution at the solution points first and then interpolating the filtered quantities at the flux points using the same Lagrange polynomials used to reconstruct the fluxes (cf. Equations (10)–(12)).

Considering for simplicity the 1D SD element depicted schematically in Figure 2, a particularly desirable feature in building discrete filters is that the filter stencil does not lie across elements. Moreover, the non-uniform spacing of the solution points should be taken into account. The preceding considerations lead to the particularly challenging task of designing asymmetric non-uniform discrete filters with a fixed cutoff length scale. For instance, for $N = 4$ (cf. Figure 2), four discrete filters G_1, G_2, G_3, and G_4 need to be built—acting on the four non-uniformly spaced solution points—none of them being symmetric. These four filters should, in principle, have sufficiently similar kernels.

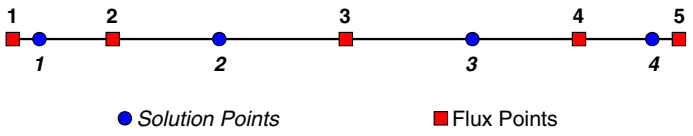

Figure 2. Schematic representation of the one-dimensional distribution of solution and flux points within the spectral difference element for $N = 4$.

DOI: 10.1002/fld

In the most general non-symmetric case, a discrete filter can be defined as [58]

$$\overline{\phi}_i = \sum_{l=-K_i}^{L_i} w_l^i \phi_{i+l}, \tag{23}$$

where the filtered quantity $\overline{\phi}_i$ is obtained as a weighted sum, with weights w_l^i of the discrete values of ϕ over the non-symmetric stencil defined by the parameters K_i and L_i. For the SD element depicted in Figure 2, the aforementioned discrete filtering operator is readily applicable. For the case of hexahedral elements as in the present study, the generalization to three dimensions follows immediately by tensor product of 1D filtering operators.

Therefore, starting from Equation (23), the filtering operator acting on the sth solution point is defined as

$$\overline{\phi}_s = \sum_{i=1}^{N} w_i^s \phi_i, \quad (s = 1\ldots., N). \tag{24}$$

The relevant spectral signature is characterized by its associated transfer function, or kernel, in Fourier space [59, 60], which is readily obtained as

$$\widehat{G}_s(k) = \sum_{i=1}^{N} w_i^s \exp\left(-\mathrm{j}\beta_i^s k\Delta\right), \quad \text{with} \quad \beta_i^s = \frac{\xi_i - \xi_s}{\Delta}, \tag{25}$$

where k is the wavenumber, $\mathrm{j} = \sqrt{-1}$, is the imaginary constant, ξ_s represents the location of the solution points, whereas $\Delta = 1/N$ is the actual resolution in computational space within the SD element (cf. Equation (20)).

A possible strategy to build discrete filters can be devised by exploiting the resolution properties of polynomials of different orders, thus performing the explicit filtering operation by applying the restriction–prolongation (RP) technique in each computational cell or similar techniques involving projection of the solution onto lower-order basis functions [22, 36, 37]. Unfortunately, these procedures are not optimal for two main reasons: (i) the filter cutoff length scale cannot be determined *a priori*, and hence, a certain level of uncertainty is introduced regarding the model behavior; and (ii) depending on the order N selected for the computation, the real part of the kernels of the filter may show undesirable over-shoots.

By using Equation (25), for instance, the real part of the Fourier transform of the discrete filters constructed using the RP technique [22] for N ranging from 3 to 6 is plotted in Figure 3 as a function of the scaled wavenumber $k\Delta/\pi \in [0:1]$. The box filters in physical space with cutoff length equal to 2Δ and 3Δ are also represented for reference. As can be seen from the figure, the cutoff frequency (namely, the frequency at which $\widehat{G}_s(k) \simeq 0.5$) of the filtering operator, which is applied to each solution point, is different, and therefore, the overall effective cutoff frequency is unpredictable. Furthermore, for $N \geqslant 4$, the most asymmetric filters, i.e. those represented with solid lines, have a relatively pronounced over-shoot in the low frequency range, a feature that may lead to non-physical growth of energy [58]. In particular, for $N = 3$ (cf. Figure 3(a)), the RP discrete filters, although free from over-shoots, are not characterized by a suitable cutoff length scale for a mixed similarity SGS model, which is typically in the range Δ–2Δ [35], and the effective cutoff length scale is $\sim 2.2\Delta$ at the central solution point and increases up to about 3.3Δ at the outermost solution points, as can be appreciated by comparison with the reference box filters.

For these problems to be overcome, two classes of discrete filters satisfying a selected set of conditions have been developed for the SD method. The first type of constrained discrete filter (hereafter indicated as CD1) takes advantage of the fact that the solution points are Gauss–Legendre quadrature points and features strictly positive weighting coefficients, whereas the second type of filter (CD2) offers the flexibility of being applicable to arbitrary distributions of points and is based on the work of Vasilyev *et al.* [58].

DOI: 10.1002/fld

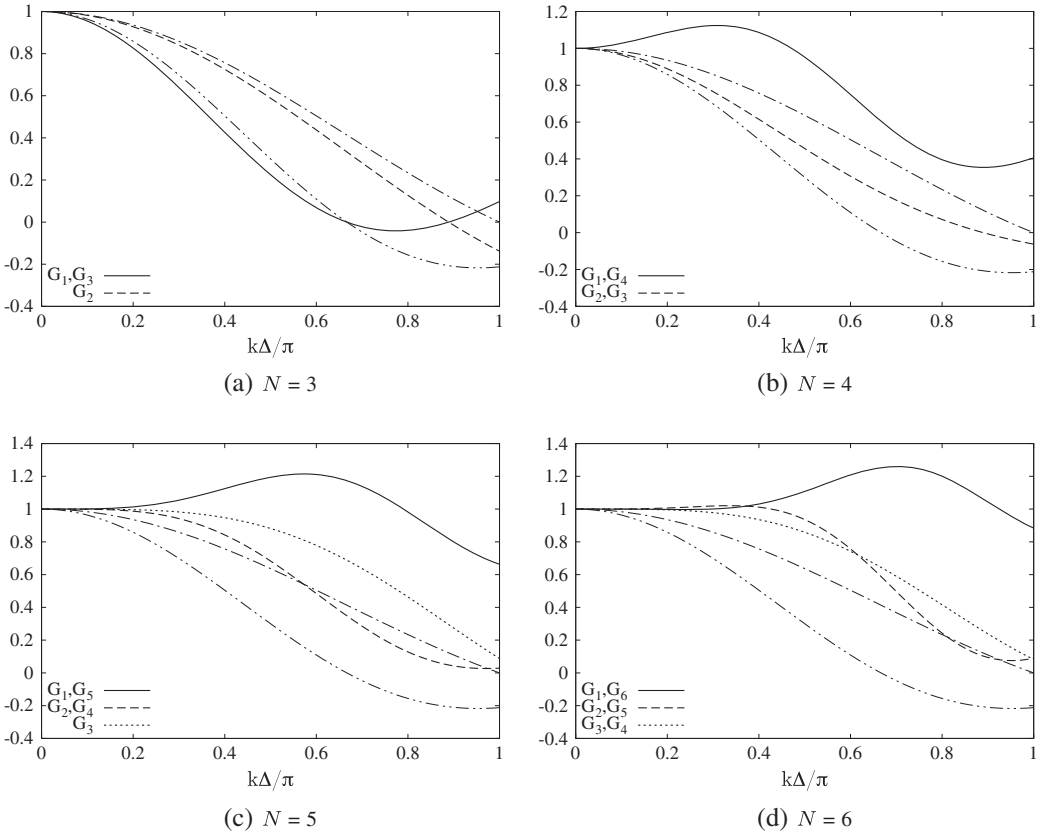

Figure 3. Real part $\mathrm{Re}[\widehat{G}(k\Delta/\pi)]$ of the Fourier transform of the restriction–prolongation (RP) discrete filters [22] for different spectral difference discretization orders N (—·— , box filter in physical space with cutoff length scale of 2Δ; —··— , box filter in physical space with cutoff length scale of 3Δ).

The real parts of the kernels of CD1 and CD2 filters for SD elements of order 3 to 6 are plotted in Figures 4 and 5, respectively. The mathematical details of their implementation are discussed in the two following sections. It is worth anticipating that, in the low frequency range, both CD1 and CD2 filters approximate the reference filter much more accurately than the RP filters (cf. Figure 3). More pronounced deviations are only observed at length scales close to Δ (i.e., $k\Delta/\pi > 1$). However, recalling that $\Delta \sim O(1/N)$, we do not expect these small scales to play a significant role as they are not supported by the actual resolution of the SD element (see [18] for details about dispersion and dissipation characteristics of the SD scheme). The actual cutoff frequency is also more predictable throughout the SD element. Moreover, the over-shoots observed in the asymmetric filters constructed by the RP method are now completely suppressed; hence, a better numerical behavior in terms of stability is expected. Indeed, numerical tests up to $N = 7$ did not exhibit any numerical instability because of the filtering procedure (cf. Section 3).

2.3.1. Constrained discrete filters by Gauss quadrature integration (CD1). By exploiting the properties of the Gauss–Legendre quadrature points, a discrete filter is obtained by analytical integration of a selected filter kernel. In particular, the 1D discrete filter is obtained under the assumption that the convolution integral can be approximately restricted within the SD element,

$$\overline{\phi}(\eta) = \int_{-\infty}^{+\infty} \phi(\xi) G_\Delta(\eta - \xi) \mathrm{d}\xi \simeq \sum_{i=1}^{N} w_i^{\mathrm{G}} \phi_i G_\Delta(\eta - \xi_i), \tag{26}$$

where G_Δ is the convolution kernel associated with the filter operation at cutoff length Δ and w_i^{G} is the Gaussian quadrature weights associated with the N solution points ξ_i. When the Gaussian filter

DOI: 10.1002/fld

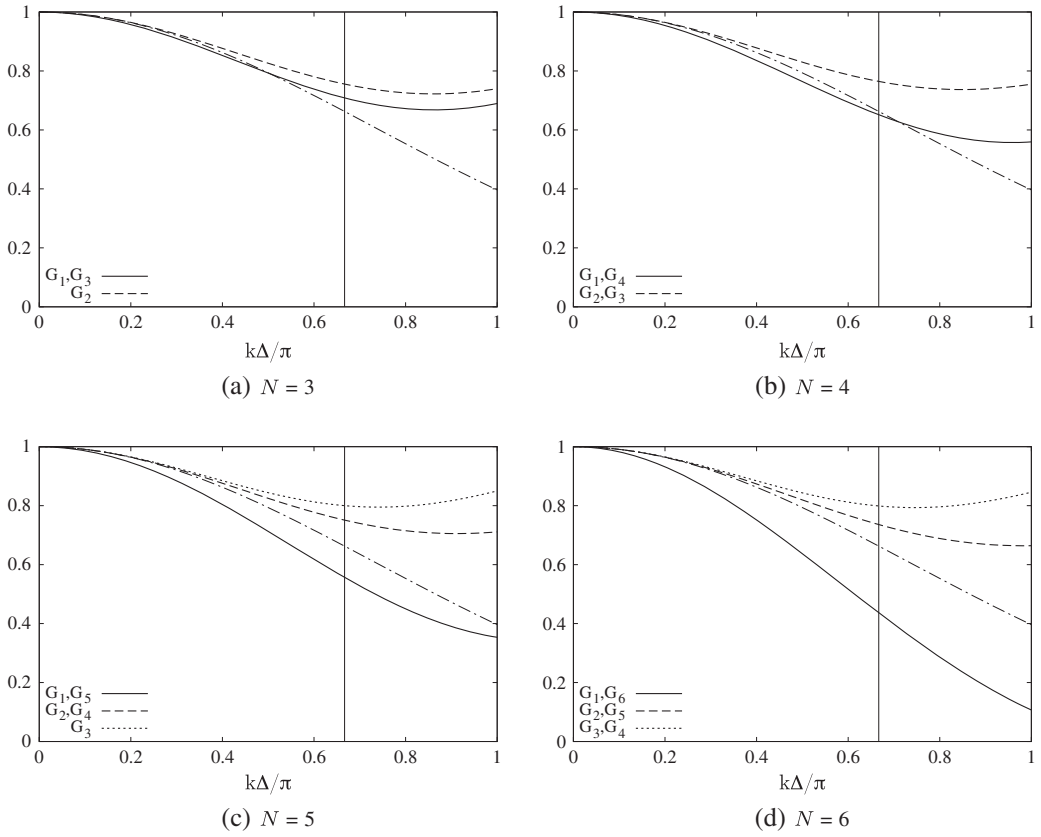

Figure 4. Real part $\mathrm{Re}[\widehat{G}(k\Delta/\pi)]$ of the Fourier transform of the first type of constrained discrete filters (CD1) for different spectral difference discretization orders N (—·— , Gaussian filter). The vertical line indicates the cutoff length scale at 1.5Δ.

[47] is chosen, the preceding integral is evaluated at each solution point as

$$\overline{\phi}_s = K \sum_{i=1}^{N} w_i^{\mathrm{G}} \phi_i \exp\left[-\Gamma \left(\frac{\xi_s - \xi_i}{\alpha_s \Delta}\right)^2\right], \quad (s = 1, \ldots, N), \tag{27}$$

where Γ is generally taken to be equal to 6, K is a normalization coefficient, and $\alpha_s\Delta$ is the desired cutoff length scale. By comparing Equations (24) and (27), the discrete filter weights are immediately obtained as

$$w_i^s = K w_i^{\mathrm{G}} \exp\left[-\Gamma \left(\beta_i^s/\alpha_s\right)^2\right], \tag{28}$$

with β_i^s given from Equation (25). Because the Gauss quadrature weights are strictly positive, the resulting filter weights are all positive as well, thus making this filter particularly well behaved for numerical simulations.

The parameter α_s, in particular, is iteratively determined beforehand for each of the N solution points, such that the estimate of the actual cutoff length of the filter, estimated from the second-order moment of the filter kernel [61, 62], is as close as possible to the selected value of $\alpha_0 = 1.5$,

$$\frac{\alpha_0^2}{12} = \sum_{i=1}^{N} w_i^s(\alpha_s) \left(\beta_i^s - \xi_m\right)^2, \quad (s = 1, \ldots, N), \tag{29}$$

with $\xi_m = \sum_{i=1}^{N} w_i^s(\alpha_s)\beta_i^s$ (the dependance of the filter weights to the parameter α_s has been explicitly indicated for clarity). Finally, the normalization coefficient is computed such that the

DOI: 10.1002/fld

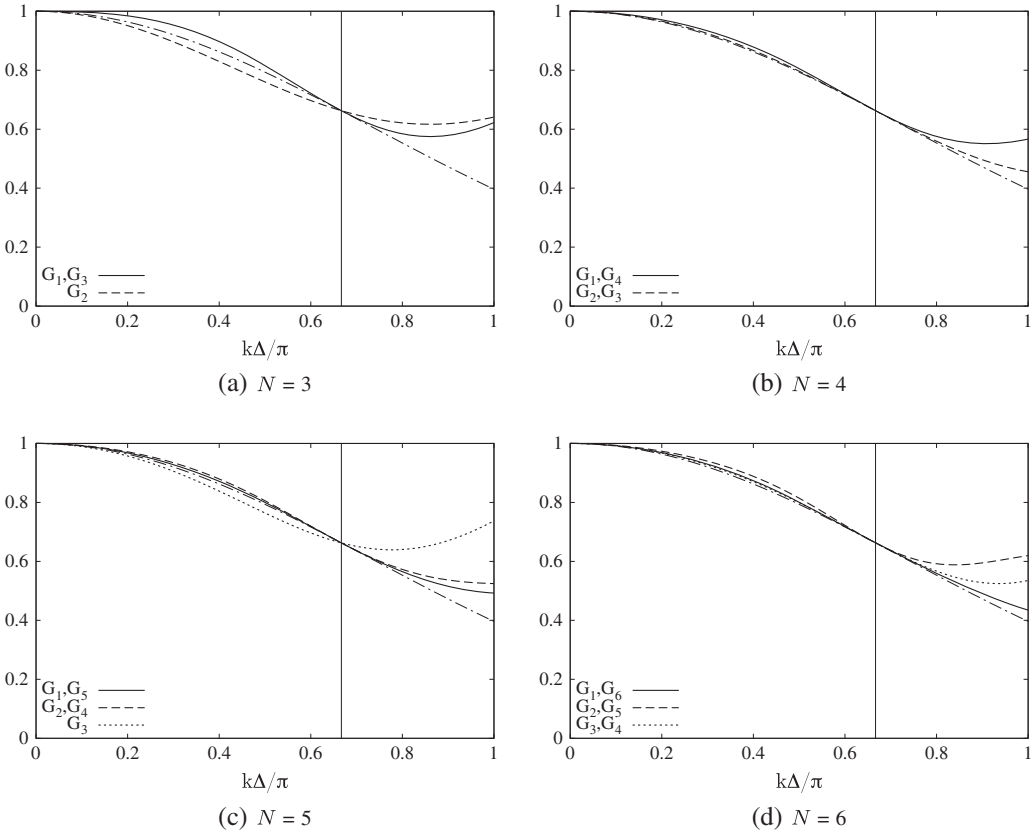

Figure 5. Real part Re$[\widehat{G}(k\Delta/\pi)]$ of the Fourier transform of the second type of constrained discrete filters (CD2) for different spectral difference discretization orders N (—·— , Gaussian filter). The vertical line indicates the cutoff length scale at 1.5Δ.

preservation of a constant property is satisfied:

$$\sum_{i=1}^{N} w_i^s = K \sum_{i=1}^{N} w_i^{\mathrm{G}} \exp\left[-\Gamma \left(\beta_i^s/\alpha_s\right)^2\right] = 1. \tag{30}$$

The real part of the kernels of CD1 filters for SD elements of order 3 to 6 is plotted in Figure 4.

2.3.2. Constrained discrete filters for arbitrarily distributed points (CD2). The method used to derive these filters is based on the work of Vasilyev *et al.* [58]. In particular, starting from Equation (25), the N filter weights w_i^s for the sth solution point can be determined by providing N constraints. More precisely, a first obvious condition is related to the preservation of a constant quantity, namely,

$$\sum_{i=1}^{N} w_i^s = 1. \tag{31}$$

Then, starting from the idea of building filters whose kernels are as close as possible to that characterizing a selected analytical filter $\widehat{G}_{\Delta_c}(k)$ with cutoff $\Delta_c = \alpha\Delta$ (e.g., the box filter in physical space or the Gaussian filter), the following condition is enforced

DOI: 10.1002/fld

$$\mathrm{Re}[\widehat{G}_s(k_c)] = \sum_{i=1}^{N} w_i^s \cos\left(\beta_i^s k_c \Delta\right) = \mathrm{Re}[\widehat{G}_{\Delta_c}(k_c)], \tag{32}$$

with

$$\mathrm{Re}[\widehat{G}_{\Delta_c}(k_c)] = \begin{cases} \left.\dfrac{\sin(k\Delta_c/2)}{k\Delta_c/2}\right|_{k=k_c} = \dfrac{2}{\pi}, & \text{for the box filter,} \\ \left.\exp\left(\dfrac{-\Delta_c^2 k^2}{4\Gamma}\right)\right|_{k=k_c} = \exp\left(\dfrac{-\pi^2}{24}\right), & \text{for the Gaussian filter,} \end{cases} \tag{33}$$

where $k_c = \pi/\Delta_c$ and the typical value $\Gamma = 6$ is selected for the Gaussian filter [47]. Equations (32) and (33) provide an explicit condition on the cutoff length scale of the resulting discrete filter operator. The remaining conditions are obtained by constraining the discrete filter to have $N-2$ vanishing moments, thus achieving formal commutation with difference operators [58].

The real part of the kernels of CD2 filters for SD elements of order 3 to 6 is plotted in Figure 5.

3. RESULTS AND DISCUSSION

In this section, the results obtained with the actual implementation of the WSM model are presented. Channel flow computations were performed at different orders ($N = 4$, 5, and 6) at three different Reynolds numbers, namely, $\mathrm{Re}_\tau = 180$, 395, and 590 (based on the friction velocity u_τ and channel half-width δ), and Mach number 0.3. Although the present method has been developed for compressible flow simulations, validation has been performed using the classical incompressible direct numerical simulation (DNS) dataset of Moser *et al.* [63]. Tests with lower Mach numbers were also performed. These were computationally expensive because of the severe time-step restriction on the explicit time integration scheme used but confirmed the absence of significant compressibility effects at Mach 0.3. Indeed, the variation in density at this Mach number is so small (about 1.4% change from the wall to the center of the channel) that the relevant impact is negligible. Notwithstanding the hardly noticeable effect, for consistency with the compressible nature of the computations, average profiles of velocity are Van Driest corrected, and Reynolds stresses are represented in semi-local coordinates (cf. [64–66] for details). It is worth recalling that, according to Foysi *et al.* [67], differences in profiles between compressible and incompressible computations are principally due to the decrease of the mean density and increase of the mean viscosity from wall values. Here, the viscosity is a prescribed constant. Also note that, in the paper by Foysi *et al.* [67], the results at Mach 0.3 were indistinguishable from the incompressible counterpart [63].

For comparison, the results of implicit LES computations (i.e., with no SGS model) are also presented. In all the computations presented in the following, the three coordinate axes x_1, x_2, and x_3 are oriented in the streamwise, wall-normal, and spanwise directions, respectively. Standard wall-normalized variables are indicated with the $+$ superscript as customary done, whereas the $*$ superscript is used to indicate semi-local normalized quantities.

3.1. Computations on structured Cartesian grids

Grid dimensions, resolution in wall units (which are obtained after normalizing with the viscous length $\ell_\tau = \nu/u_\tau$), and total number of degrees of freedom (DOF) for the three Reynolds numbers are summarized in Table I. The resolution of the grids, in particular, was estimated as the actual element size divided by the number of solution points used within the element; in a finite volume context, this would be equivalent to assuming that each element is filled with N^3 control volumes. It should be noted that, because of the clustering of solution points close to the element interfaces for the actual Gauss–Legendre quadrature points, the location of the first solution point in the wall-normal direction can be estimated by multiplying the minimum Δ_2^+ from Table I by 0.28, 0.23, and 0.20 for $N = 4$, 5, and 6, respectively (the actual location of the first solution point can also be checked on the plots when wall units are used on the abscissa).

DOI: 10.1002/fld

Table I. Grid size and resolution for channel flow computations (resolution is estimated as the element size divided by the number of solution points).

	Re_τ	Re_m	$L_1 \times L_3$	$n_1 \times n_2 \times n_3$	N	DOF	Δ_1^+	Δ_2^+	Δ_3^+
CHN1	180	5,930	$4\pi\delta \times 2\pi\delta$	$15 \times 15 \times 15$	4	2.2×10^5	38	2.0–10	19
CHN2			$4\pi\delta \times 2\pi\delta$	$12 \times 12 \times 12$	5	2.2×10^5	38	2.0–10	19
CHN3	395	14,130	$2\pi\delta \times 1\pi\delta$	$16 \times 12 \times 12$	4	1.5×10^5	39	1.2–43	26
CHN4			$2\pi\delta \times 1\pi\delta$	$13 \times 9 \times 9$	5	1.3×10^5	38	2.1–33	28
CHN4*			$2\pi\delta \times 1\pi\delta$	$39 \times 27 \times 27$	5	3.6×10^6	12	1.7–10	9
CHN5	590	22,260	$4\pi\delta \times 1\pi\delta$	$24 \times 15 \times 15$	5	6.8×10^5	62	2.3–32	25
CHN6			$4\pi\delta \times 1\pi\delta$	$20 \times 12 \times 12$	6	6.2×10^5	62	3.4–33	26

$\mathrm{DOF} = (n_1 \times n_2 \times n_3) \times N^3$.

All the computations were performed with periodic boundary conditions in the streamwise and spanwise directions, and no-slip isothermal walls were used on the top and bottom planes. To drive the flow, a source term $\boldsymbol{\mathcal{S}} = |\det(\boldsymbol{J})|\boldsymbol{S}$, with $\boldsymbol{S} = \begin{pmatrix} 0 & s_2 & 0 & 0 & s_5 \end{pmatrix}^{\mathrm{T}}$, was added to the right-hand side of Equation (4). In particular, given the compressible nature of the solver, the source term s_2 was determined at each time step to equilibrate the instantaneous resultant shear at the wall F_{w}; a relaxation term toward the expected mass flow rate $\dot{m}_0$ was also included to accelerate convergence,

$$s_2 = \frac{F_{\mathrm{w}}}{V} - \frac{\alpha}{\Delta t}(\dot{m} - \dot{m}_0), \tag{34}$$

where $V = L_1 L_2 L_3$ is the volume of the computational domain and the relaxation coefficient α was tentatively set to 0.3, a value that produced a relatively fast convergence without compromising stability. The mass flow rate was computed as

$$\dot{m} = \frac{1}{2\delta}\int_{-\delta}^{\delta} \langle \rho u_1 \rangle \mathrm{d}x_2, \tag{35}$$

where $\langle \cdot \rangle$ represents averaging in the streamwise and spanwise directions. In order to account for the work done by the uniform driving body force s_2 the source term for the energy equation was computed as the product of s_2 and the bulk velocity [68], that is,

$$s_5 = u_{\mathrm{b}} s_2, \quad \text{with} \quad u_{\mathrm{b}} = \dot{m}\left[\frac{1}{2\delta}\int_{-\delta}^{\delta} \langle \rho \rangle \mathrm{d}x_2\right]^{-1}. \tag{36}$$

The computations were initialized with a uniform streamwise fourth-order velocity profile,

$$u_1(\boldsymbol{x}) = \frac{15}{8} u_0 \left[1 - \left(\frac{x_2}{\delta}\right)^2\right]^2, \tag{37}$$

and a perturbed vertical velocity component computed as

$$u_2(\boldsymbol{x}) = 0.1 u_0 \exp\left[-\left(\frac{x_1 - L_1/2}{L_1}\right)^2\right] \exp\left[-\left(\frac{x_2}{2\delta}\right)^2\right] \cos\left(4\pi \frac{x_3}{L_3}\right), \tag{38}$$

where u_0 is the reference velocity and L_1 and L_3 are the dimensions of the computational domain in the streamwise and spanwise directions, respectively [69, 70]. The flow was then left to evolve, undergo transition to turbulence, and reach the statistical steady state. The time history of the friction coefficient $c_{\mathrm{f}}(t) = 2\tau_{\mathrm{w}}(t)/\left(\rho u_{\mathrm{b}}^2\right)$, normalized by the exact expected mean value (7.38×10^{-3}, 6.25×10^{-3}, and 5.62×10^{-3} for $\mathrm{Re}_\tau = 180$, 395, and 590, respectively), is plotted in Figure 6

DOI: 10.1002/fld

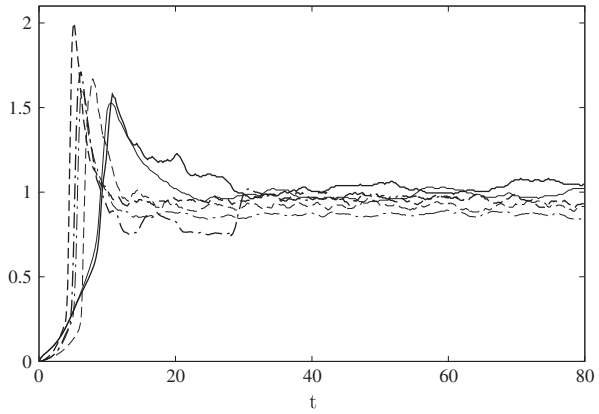

Figure 6. Time history of the normalized friction coefficient: ——— , test CHN1; ——— , test CHN2; – – – – – , test CHN3; – – – – – , test CHN4; — · — , test CHN5; — · — , test CHN6.

Table II. Statistical samples and convergence.

	Samples	Length	$\langle u_1 \rangle_{L2}$	$\langle u_2 \rangle_{L2}$	$\langle u_1^2 \rangle_{L2}$	$\langle u_2^2 \rangle_{L2}$	$\langle u_1 u_2 \rangle_{L2}$
CHN1	9×10^6	$17.9\,T_0$	2.0×10^{-2}	6.3×10^{-3}	3.3×10^{-3}	3.8×10^{-4}	6.7×10^{-4}
CHN2	9×10^6	$13.4\,T_0$	2.2×10^{-2}	6.8×10^{-3}	3.7×10^{-3}	4.2×10^{-4}	7.8×10^{-4}
CHN3	15×10^6	$20.6\,T_0$	7.9×10^{-3}	2.6×10^{-3}	1.3×10^{-3}	1.6×10^{-4}	2.7×10^{-4}
CHN4	14×10^6	$27.1\,T_0$	7.4×10^{-3}	2.6×10^{-3}	1.2×10^{-3}	1.7×10^{-4}	2.8×10^{-4}
CHN4*	6×10^7	$9.0\,T_0$	7.4×10^{-2}	3.6×10^{-2}	1.1×10^{-2}	2.7×10^{-3}	3.6×10^{-3}
CHN5	22×10^6	$4.9\,T_0$	3.2×10^{-2}	1.3×10^{-2}	4.9×10^{-3}	7.9×10^{-4}	1.2×10^{-3}
CHN6	21×10^6	$5.6\,T_0$	2.9×10^{-2}	1.2×10^{-2}	4.6×10^{-3}	7.4×10^{-4}	1.1×10^{-3}

T_0 represents the flow-through time, L_1/u_b; the $L2$-norms are obtained from Equation (39).

for the six test cases. As can be observed, all the computations reached the statistical steady state. Note that the sudden change in c_f for test CHN6 at $t \sim 30$ was due to the scheme being switched from order 4 to the final value of 6 to accelerate convergence.

After the flow field was fully developed and established, a number N_t of statistical samples were collected in time; further, ensemble averaging in the streamwise and spanwise directions was also performed. Global statistical convergence was checked continuously by calculating the $L2$-norm of the change in the statistical quantity $\langle \phi \rangle$ of interest between two successive samplings n and $n-1$ as

$$\langle \phi \rangle_{L2}^{\{n\}} = \left[\sum_{i,j,k} \left(\langle \phi \rangle_{i,j,k}^{\{n\}} - \langle \phi \rangle_{i,j,k}^{\{n-1\}} \right)^2 \right]^{1/2}, \tag{39}$$

where the summation is extended to the whole computational domain. The total number of samples, computed as $N_t \times N \times (n_1 \times n_3)$, the length of the time-averaging procedure, and the $L2$-norms relevant to first-order and second-order statistical moments of velocity are summarized in Table II.

A first check regarding the behavior of the proposed discrete filters is reported by comparing the results obtained with the WSM model in conjunction with different discrete filtering approaches, that is, using the CD1, CD2, and RP filters (cf. Section 2.3). The relevant results are shown in Figure 7 for the test case $\mathrm{Re}_\tau = 395$, $N = 4$ (CHN3). The proposed CD1—for this filter, the relevant results correspond to those shown in Figures 8–9(c)—and CD2 filters give almost identical

DOI: 10.1002/fld

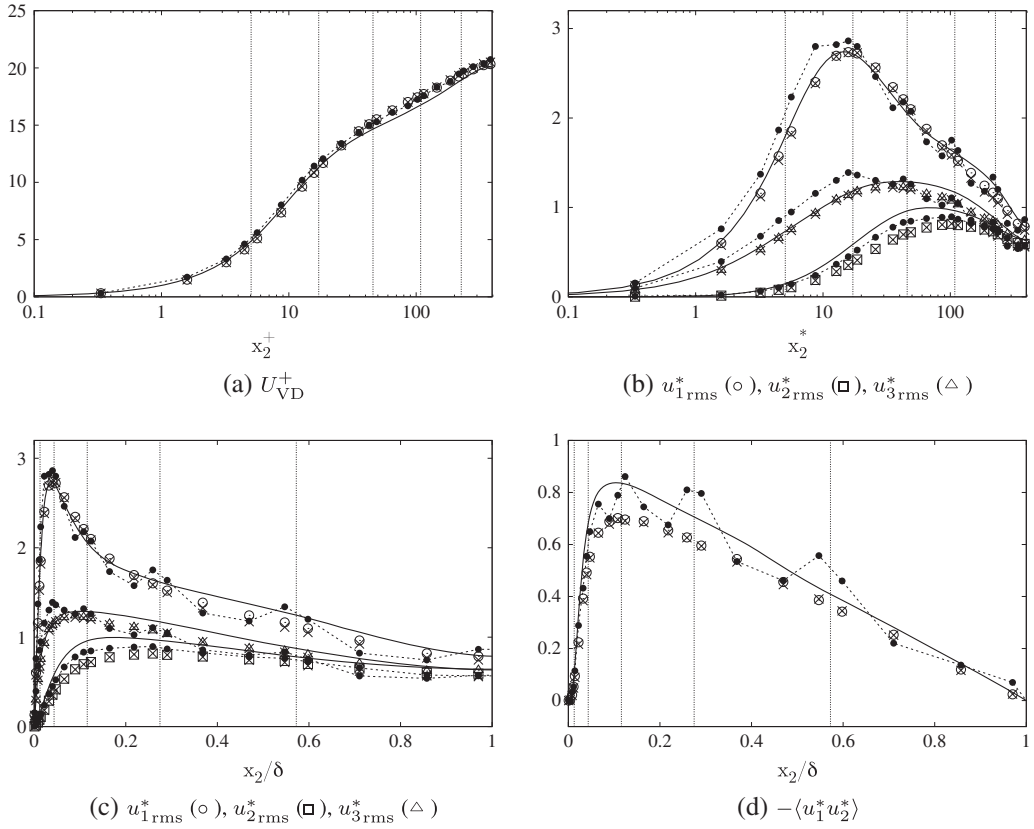

(a) U^+_{VD} (b) $u^*_{1\mathrm{rms}}$ (○), $u^*_{2\mathrm{rms}}$ (□), $u^*_{3\mathrm{rms}}$ (△)

(c) $u^*_{1\mathrm{rms}}$ (○), $u^*_{2\mathrm{rms}}$ (□), $u^*_{3\mathrm{rms}}$ (△) (d) $-\langle u^*_1 u^*_2 \rangle$

Figure 7. Resolved mean velocity profile (a), root mean square of velocity fluctuations (b, c), and Reynolds shear stresses (d) for the case $\mathrm{Re}_\tau = 395$, $N = 4$ (CHN3): open symbols, LES with WSM model and the first type of discrete filter (CD1); ×, LES with WSM model and second type of discrete filter (CD2); •, LES with WSM model and restriction–prolongation (RP) filter; solid lines, DNS data [63]. The actual location of element interfaces is indicated by vertical lines.

results and in very good agreement with DNS data. As mentioned in the previous section, CD1 filters have the advantage of being strictly positive but require a specific distribution of solution points in the element (i.e., Gauss–Legendre quadrature points), whereas the CD2 filters offer the additional flexibility of being applicable to arbitrary distributions of solution points, hence enabling accurate explicit filtering in a broad range of similar high-order schemes.

The RP filter of order 4, which corresponds to a sharp cutoff in modal space, produces results that are much less satisfactory, especially in terms of second-order statistical moments, where a very marked and unphysical oscillatory behavior of the solution is observed across the interfaces of the elements (indicated in the plots by vertical dotted lines). This behavior is most probably to be ascribed to the quite different cutoff frequencies characterizing these filters within the element and to the low-frequency over-shoots observed in the kernels connected with the first and last solution points of each element (cf. Figure 3(b)). The situation is expected to become worse when the polynomial order is increased because over-shoots in the kernels become stronger and start to appear for interior solution points as well.

First-order and second-order statistical moments from explicit LES with the WSM model (using CD1 filter) and implicit LES for the three Reynolds numbers are shown in Figures 8–10. The behavior of the WSM model in reproducing the statistical features of the flow is quite satisfactory for each test case. With regard to the mean velocity profiles (Figure 8), the log law intercept is slightly overestimated with respect to the DNS value (about 5.5 for $\mathrm{Re}_\tau = 180$ and 5.0 for the other Reynolds numbers). In general, even if the DOF and spatial resolution are kept almost the same (cf. tests CHN1 and CHN2 or CHN5 and CHN6 in Table I), higher-order computations give

DOI: 10.1002/fld

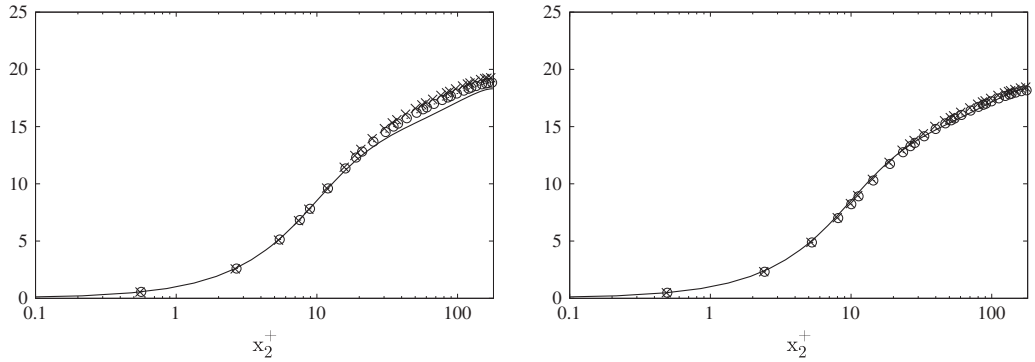

(a) CHN1: $\mathrm{Re}_\tau = 180$, $N = 4$ (b) CHN2: $\mathrm{Re}_\tau = 180$, $N = 5$

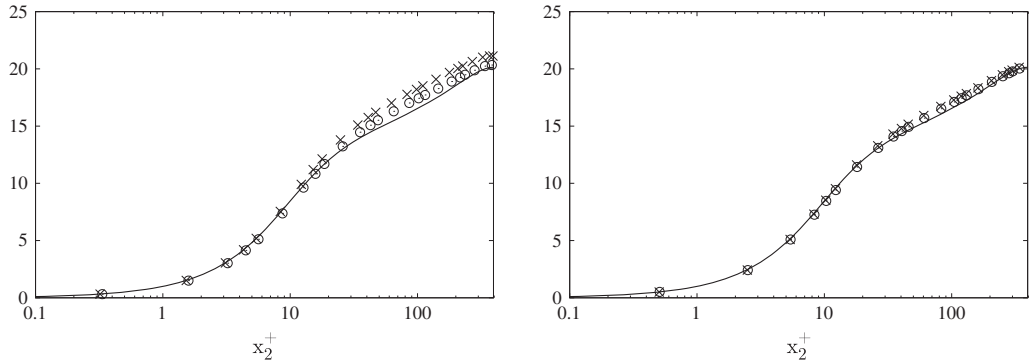

(c) CHN3: $\mathrm{Re}_\tau = 395$, $N = 4$ (d) CHN4: $\mathrm{Re}_\tau = 395$, $N = 5$

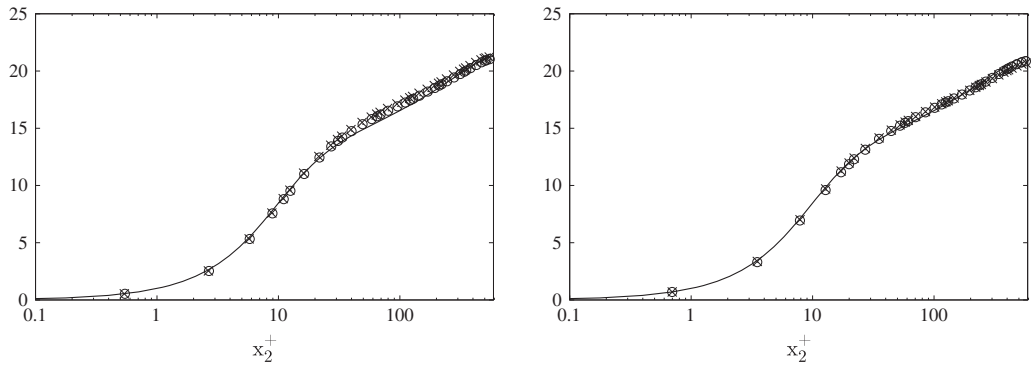

(e) CHN5: $\mathrm{Re}_\tau = 590$, $N = 5$ (f) CHN6: $\mathrm{Re}_\tau = 590$, $N = 6$

Figure 8. Resolved Van-Driest-corrected mean streamwise velocity profile U_{VD}^+: ∘ , LES with WSM model; ×, implicit LES; lines, DNS data [63].

better results than the lower-order counterparts. Overall, the use of the SGS model produces an improvement in the results obtained by implicit LES, which is mostly evident for the computations with four solution points per element. Reynolds stresses (cf. Figure 9) are most sensitive to the use of the SGS model, and implicit LES shows a marked tendency to overestimate root mean square velocity fluctuations within the buffer layer (i.e., $5 \leqslant x_2^* \leqslant 70$), especially in the streamwise direction. The profiles obtained with the WSM model are in good agreement with the DNS data, regardless of the spatial discretization order. The location and intensity of the peak of streamwise velocity fluctuation are correctly captured at the three Reynolds numbers. Spanwise and vertical resolved fluctuations tend to be underestimated at $\mathrm{Re}_\tau = 395$ and 590, which is consistent with the fact

DOI: 10.1002/fld

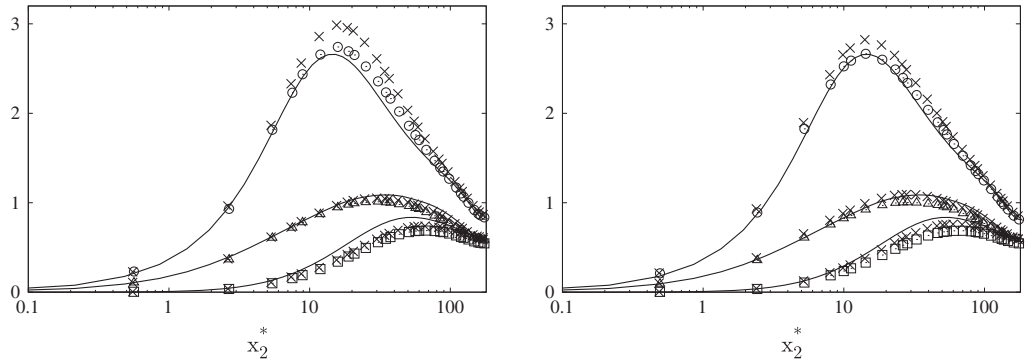

(a) CHN1: $\mathrm{Re}_\tau = 180$, $N = 4$

(b) CHN2: $\mathrm{Re}_\tau = 180$, $N = 5$

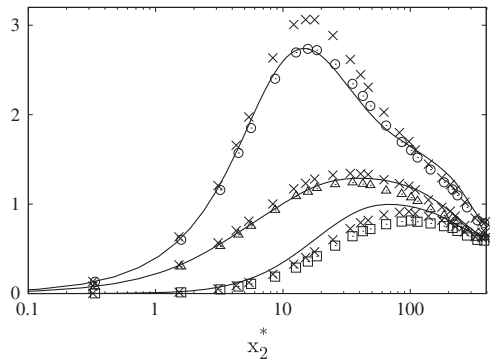

(c) CHN3: $\mathrm{Re}_\tau = 395$, $N = 4$

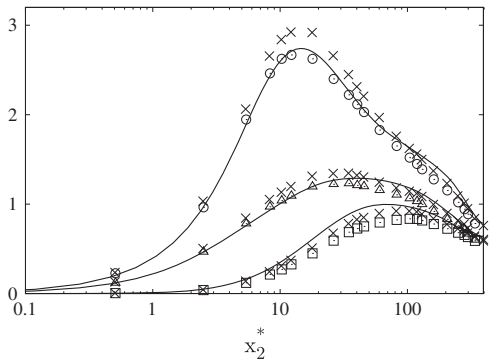

(d) CHN4: $\mathrm{Re}_\tau = 395$, $N = 5$

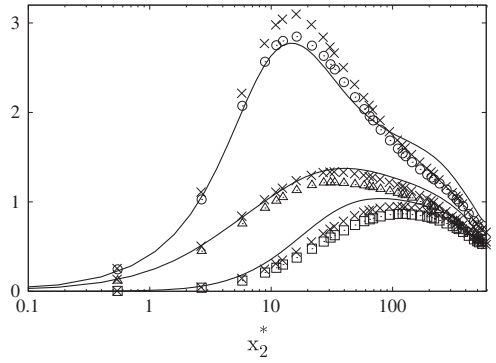

(e) CHN5: $\mathrm{Re}_\tau = 590$, $N = 5$

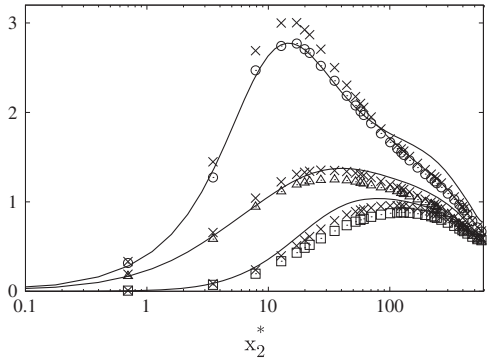

(f) CHN6: $\mathrm{Re}_\tau = 590$, $N = 6$

Figure 9. Resolved root mean square of velocity fluctuations in semi-local coordinates: open symbols, LES with WSM model; ×, implicit LES; lines, DNS data [63]. ∘ , $u^*_{1\,\mathrm{rms}}$; □ , $u^*_{2\,\mathrm{rms}}$; △ , $u^*_{3\,\mathrm{rms}}$.

that, for these Reynolds numbers, grid resolution is much lower. The vertical fluctuations are generally the most underpredicted. Also, at higher Reynolds numbers, no computation seems to be capable of predicting the correct root mean square velocities for $x_2^* > 100$ (cf. Figure 9). In this regard, it is worth recalling that the plotted results do not account for the contribution from the SGS tensor, whose action is supposedly significant in the center of the channel where, because of the grid stretching, the lowest resolution is attained (refer to discussion about sub-grid activity later in the text).

The resolved turbulent shear stresses from the LES are always below the DNS curves, whereas the results from implicit LES are much closer (cf. Figure 10). Given the close connection between

DOI: 10.1002/fld

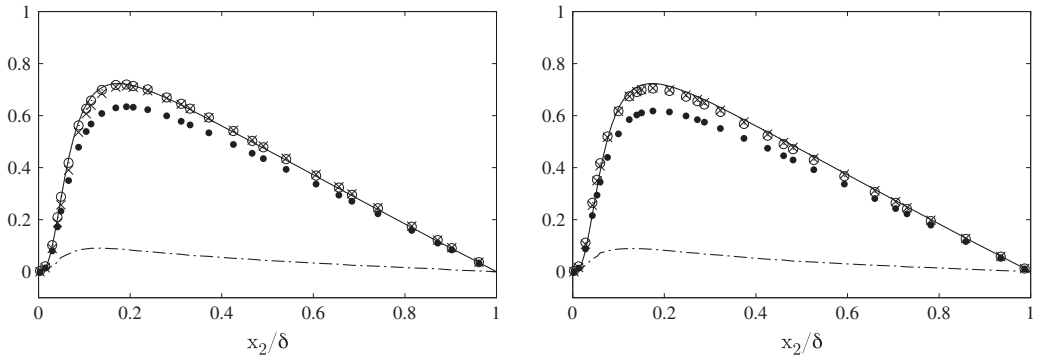

(a) CHN1: $\mathrm{Re}_\tau = 180$, $N = 4$

(b) CHN2: $\mathrm{Re}_\tau = 180$, $N = 5$

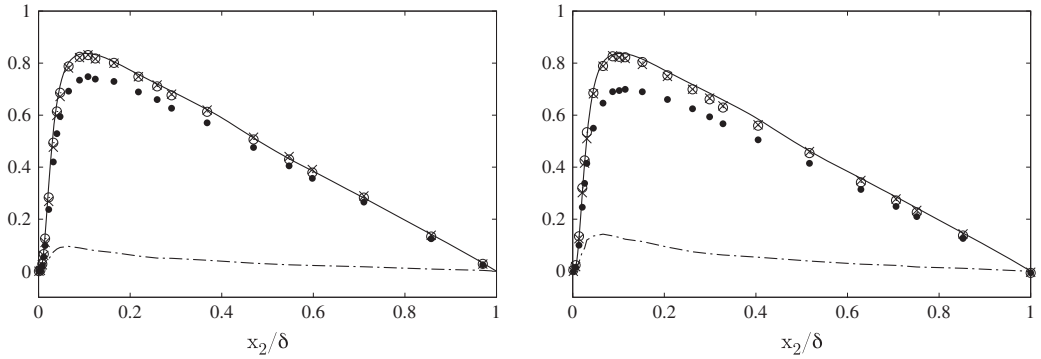

(c) CHN3: $\mathrm{Re}_\tau = 395$, $N = 4$

(d) CHN4: $\mathrm{Re}_\tau = 395$, $N = 5$

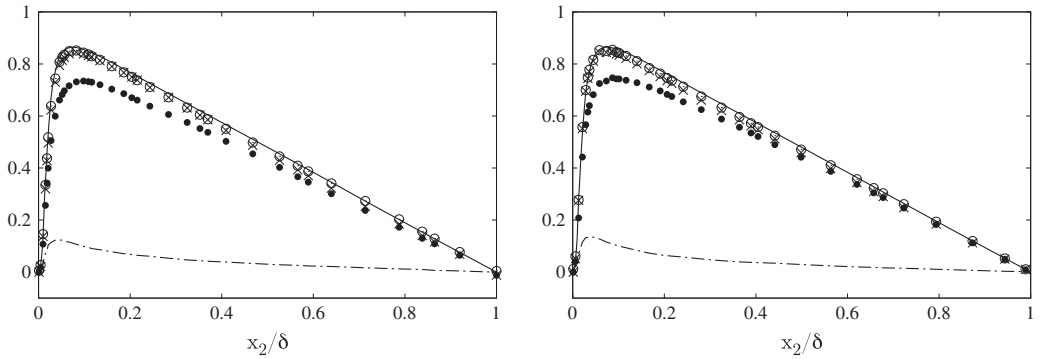

(e) CHN5: $\mathrm{Re}_\tau = 590$, $N = 5$

(f) CHN6: $\mathrm{Re}_\tau = 590$, $N = 6$

Figure 10. Reynolds shear stresses: ∘ , LES with WSM model (resolved + sub-grid scale); ×, implicit LES; solid lines, DNS data [63]; —·— , $\langle \tau_{12} \rangle$ from LES; •, resolved shear stress from LES.

the mean streamwise velocity profile and the turbulent shear stress across the channel—the two quantities are strictly related through the steady Reynolds averaged x_1 momentum equation—and given the good agreement observed for the former quantity, it is here argued that the actual global turbulent shear from LES, namely resolved + SGS modeled contribution, must be in good agreement with its DNS counterpart. In the case of explicit LES, in fact, it is the combined effect of the resolved turbulent shear and the SGS stress tensor that is actually experienced by the flow, whereas in the implicit LES, the only contribution to the turbulent shear comes from the deviator of the Reynolds stress tensor constructed on the resolved velocity field. Therefore, plotting the resolved contribution only can be misleading, especially when the grid is relatively coarse and the SGS contribution is significant. In implicit LES computations, the insufficient skin friction arising from

DOI: 10.1002/fld

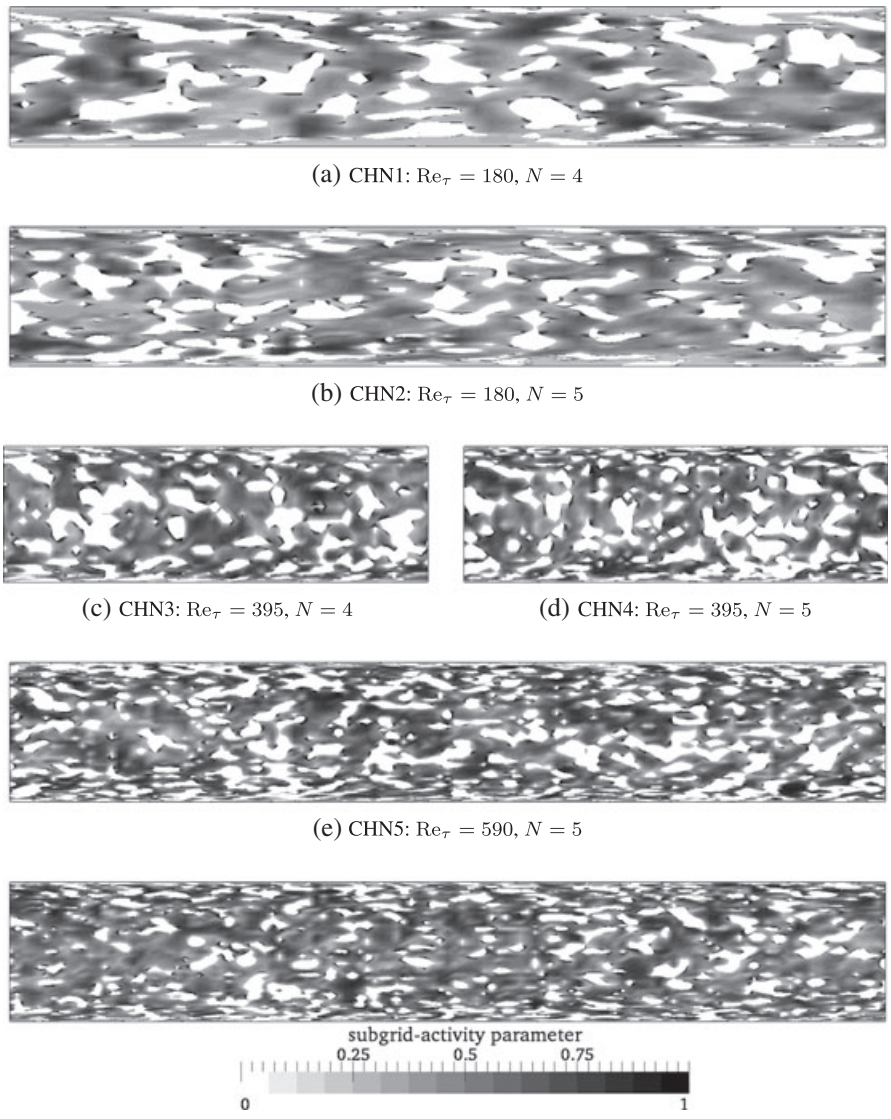

(a) CHN1: $\mathrm{Re}_\tau = 180$, $N = 4$

(b) CHN2: $\mathrm{Re}_\tau = 180$, $N = 5$

(c) CHN3: $\mathrm{Re}_\tau = 395$, $N = 4$

(d) CHN4: $\mathrm{Re}_\tau = 395$, $N = 5$

(e) CHN5: $\mathrm{Re}_\tau = 590$, $N = 5$

(f) CHN6: $\mathrm{Re}_\tau = 590$, $N = 6$

Figure 11. Contours of the instantaneous sub-grid activity parameter [71] over vertical planes.

the deficiency in fine-scale strain close to the wall must be compensated by higher levels of velocity fluctuations, whose cross-correlations happen to be very close to the DNS results. On the other hand, when the SGS model is used, the compensation mechanism comes from the SGS model itself, and the resolved velocity fluctuations are better predicted overall, such that: (i) close to the wall, where SGS model action is low, resolved fluctuations closely match DNS data; and (ii) away from wall, where SGS model contribution is significant, resolved fluctuations are underestimated, but the inclusion of the SGS term allows for the proper turbulent shear stress to be recovered. This is readily confirmed by collecting the mean SGS shear stress $\langle \tau_{12} \rangle$ during the computation and by comparing the exact turbulent shear from DNS with the approximate global (resolved + SGS) turbulent shear from LES, namely $\langle \overline{u}'_1 \overline{u}'_2 \rangle + \langle \tau_{12} \rangle$ [47]. As can be observed in Figure 10, the approximate global turbulent shear matches almost perfectly the DNS data, thus confirming that the model is correctly compensating for the insufficient shear from the resolved flow field.

Note that, for the case at $\mathrm{Re}_\tau = 180$, in particular, the results obtained from implicit LES computations on CHN1 and CHN2 grids (fourth and fifth orders, respectively) with 60^3 DOF are in

DOI: 10.1002/fld

similar agreement with the DNS data as those obtained by Visbal and Rizzetta [4] with a sixth-order compact scheme combined with a tenth-order filter and implicit second-order time integration (therein referred to as C6F10-BW2) over 61^3 points (the same geometrical dimensions for the computational grid). When the WSM model on the CHN2 grid is used, the results obtained with 60^3 DOF are essentially identical to those obtained with the C6F10-BW2 scheme on their F mesh with 91^3 points.

To better quantify the amount of modeling in the LES computations, a sub-grid activity parameter can be defined as

$$\overline{\varepsilon}_{\text{ratio}} = \frac{\langle \varepsilon_{\text{sgs}} \rangle}{\langle \varepsilon_{\text{sgs}} \rangle + \langle \varepsilon_{\mu} \rangle}, \tag{40}$$

where $\varepsilon_{\text{sgs}} = \tau_{ij}^{\text{d}} \tilde{A}_{ij}$ measures the dissipation from the SGS stress tensor and $\varepsilon_{\mu} = 2\overline{\mu} \tilde{A}_{ij} \tilde{A}_{ij}$ measures the molecular dissipation. By definition, $\overline{\varepsilon}_{\text{ratio}} \in [0 : 1)$, with $\overline{\varepsilon}_{\text{ratio}} = 0$ corresponding to DNS and $\overline{\varepsilon}_{\text{ratio}} \to 1$ for an LES at infinite Reynolds number [71]. An instantaneous sub-grid activity parameter is also defined as

$$\varepsilon_{\text{ratio}}(\boldsymbol{x}, t) = \frac{\varepsilon_{\text{sgs}}}{\varepsilon_{\text{sgs}} + \varepsilon_{\mu}} = \frac{\nu_{\text{ratio}}}{1 + \nu_{\text{ratio}}}, \tag{41}$$

where $\nu_{\text{ratio}} = \varepsilon_{\text{sgs}}/\varepsilon_{\mu}$ is the normalized SGS energy transfer coefficient [33]. Note that ν_{ratio} reduces to the ratio ν_{sgs}/ν for an eddy viscosity model and becomes negative in regions characterized by backward SGS energy transfer. Regions of negative SGS energy transfer shall not be accounted for when computing $\varepsilon_{\text{ratio}}$ with Equation (41), which is strictly valid for purely dissipative models only. Instantaneous contours of the sub-grid activity parameter are presented in Figure 11, where blank regions indicate locations where the SGS model is either inactive or backscattering. In all the six computations, the SGS model appears to be relatively active, with values of instantaneous sub-grid activity as high as 0.5–0.75. The average sub-grid activity, on the other hand, was generally lower (cf. Figure 12). Values of $\overline{\varepsilon}_{\text{ratio}}$ in the outer layer were in the range 0.18–0.26 for CHN1 and CHN2, 0.25–0.4 for CHN3 and CHN4, and 0.3–0.43 for CHN5 and CHN6. As expected, $\langle \varepsilon_{\text{sgs}} \rangle$ was always strictly positive, thus confirming that, despite the presence of local events of reverse energy transfer, the SGS model shows a dissipative behavior (in average). A similar sub-grid activity was observed for the two computations of each Reynolds number, which is consistent with the fact that the same overall resolution was maintained when changing the order of the solution (cf. Table I).

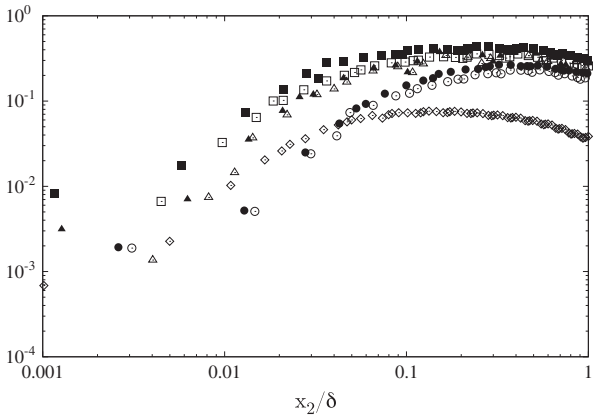

Figure 12. Average sub-grid activity parameter [71]: ○ , CHN1 (open), CHN2 (solid); △ , CHN3 (open), CHN4 (solid); ◇ , CHN4*; □ , CHN5 (open), CHN6 (solid).

DOI: 10.1002/fld

To check the numerical convergence when the grid is refined, the $\mathrm{Re}_\tau = 395$ at $N = 5$ test case was repeated on a relatively fine mesh. The relevant details about grid spacing and DOF are reported in Table I and labeled as CHN4*. The equivalent maximum grid spacing for this mesh, which has about 4×10^6 DOF, is about 10 wall units in the three directions, with the first solution point at about $\Delta_2^+ = 0.4$ from the wall (i.e., 1.7 times the correction coefficient 0.23 for the fifth-order case). The comparison with the coarse-mesh computation, namely CHN4, is shown in Figure 13. Not surprisingly, the agreement of the fine-mesh computation with the DNS data is excellent, thus confirming very good convergence of the numerical scheme and the implemented model when grid resolution is increased. Note that the DNS computation by Moser *et al.* [63] was performed with a mesh of identical geometrical dimensions, but with about 9.5×10^6 DOF. In this respect, the present computation can be considered as a relatively fine LES. The relevant sub-grid activity was in the range 0.04–0.08 (cf. Figure 12), and the mean SGS shear stress $\langle\tau_{12}\rangle$ is almost 0 throughout the channel, with a very low peak of about 0.03. The corresponding maximum value measured on the coarse mesh was about five times higher (Figure 14). For the fine-mesh computation, the SGS shear stress is also much more localized around the buffer layer and goes rapidly to (almost) 0 above it, whereas in the coarse-mesh computation, significant SGS shear is observed even in the logarithmic region. As can be observed in Figure 14, above $x_2^* = 100$, the SGS shear on the coarse grid is everywhere more than 10 times higher than the fine-grid counterpart.

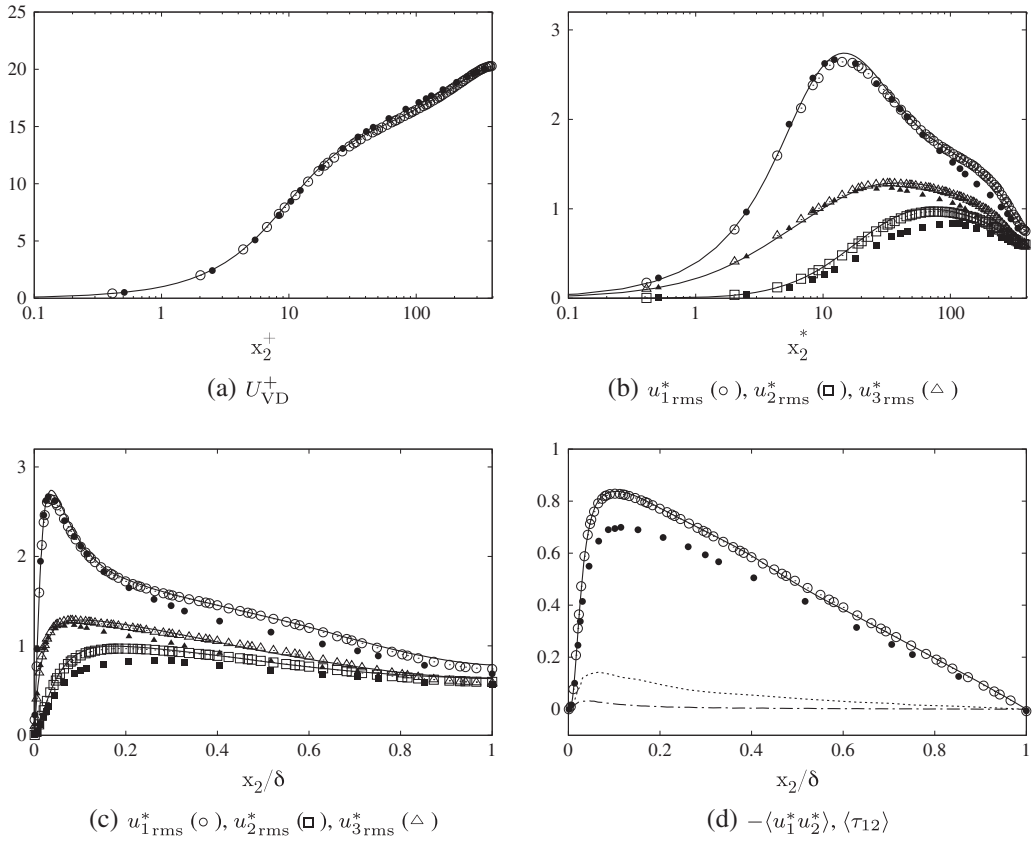

(a) U^+_{VD}

(b) $u^*_{1\mathrm{rms}}$ (○), $u^*_{2\mathrm{rms}}$ (□), $u^*_{3\mathrm{rms}}$ (△)

(c) $u^*_{1\mathrm{rms}}$ (○), $u^*_{2\mathrm{rms}}$ (□), $u^*_{3\mathrm{rms}}$ (△)

(d) $-\langle u_1^* u_2^*\rangle$, $\langle\tau_{12}\rangle$

Figure 13. Resolved mean velocity profile (a), root mean square of velocity fluctuations (b, c), and Reynolds shear stresses (d) for cases CHN4 and CHN4*: open symbols, LES with WSM model and the first type of discrete filter (CD1) on fine mesh (CHN4*); solid symbols, LES with WSM model and the first type of discrete filter (CD1) on coarse mesh (CHN4); solid lines, DNS data [63]; —·— , $\langle\tau_{12}\rangle$ on fine mesh (CHN4*); ····· , $\langle\tau_{12}\rangle$ on coarse mesh (CHN4).

DOI: 10.1002/fld

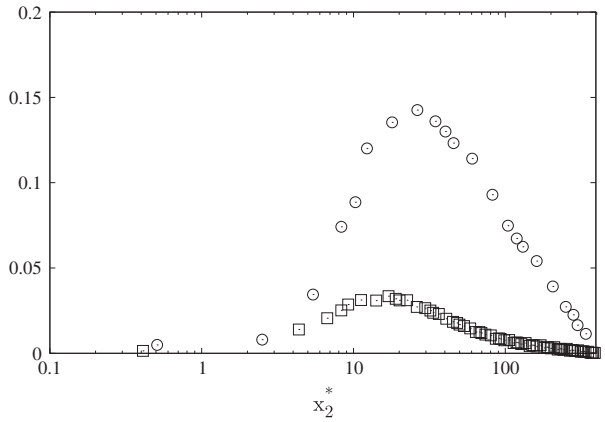

Figure 14. Mean sub-grid scale shear stress $\langle \tau_{12} \rangle$: ∘ , test case CHN4 (coarse mesh); □ , test case CHN4* (fine mesh).

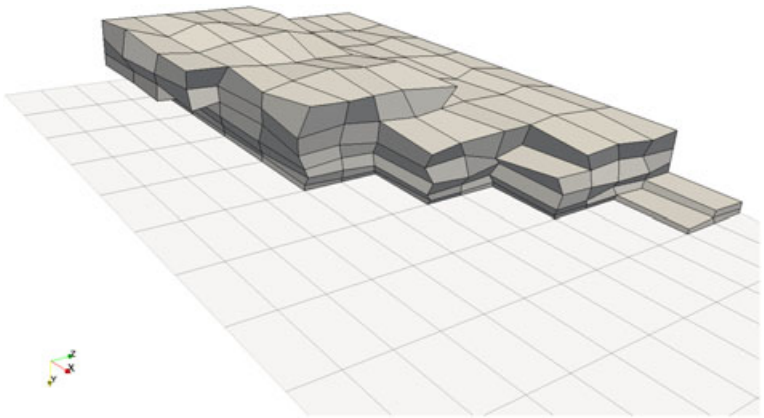

Figure 15. Randomly perturbed mesh for the test case at $\mathrm{Re}_\tau = 180$: a portion corresponding to approximately a quarter of the whole grid is represented.

3.2. Computations on unstructured grids

The long-term goal of this research is to develop LES methods for industrial applications, which typically involve very complex geometries, requiring the use of unstructured meshes. In this context, it may be noted that a tetrahedral element can be subdivided into four hexahedra, so the use of hexahedral elements is not a severe restriction.

Accordingly, to gauge the behavior of the discrete filters when the computational grid is unstructured, the test cases CHN2, CHN4, and CHN6 were repeated using randomly perturbed meshes, which were obtained from the Cartesian counterparts by displacing each interior node within a sphere of radius equal to 30% of the shortest concurrent edge. Figure 15 shows a portion of the perturbed mesh used for the $\mathrm{Re}_\tau = 180$ test case. The resolved statistical moments obtained with the WSM model and CD1 filter on the Cartesian grids—which correspond to the previous results—and on the randomly perturbed meshes are compared in Figure 16. As can be seen, the results are almost indistinguishable, thus verifying the extremely good performances of the discrete operators (and the adopted SGS model) in the case of unstructured grids. Note that, for completeness, results from implicit LES obtained on randomly perturbed meshes are also plotted. There are almost identical to previous implicit LES results computed on regular Cartesian meshes, thus giving further evidence of the extremely good capability of the numerical scheme itself in handling unstructured grids.

DOI: 10.1002/fld

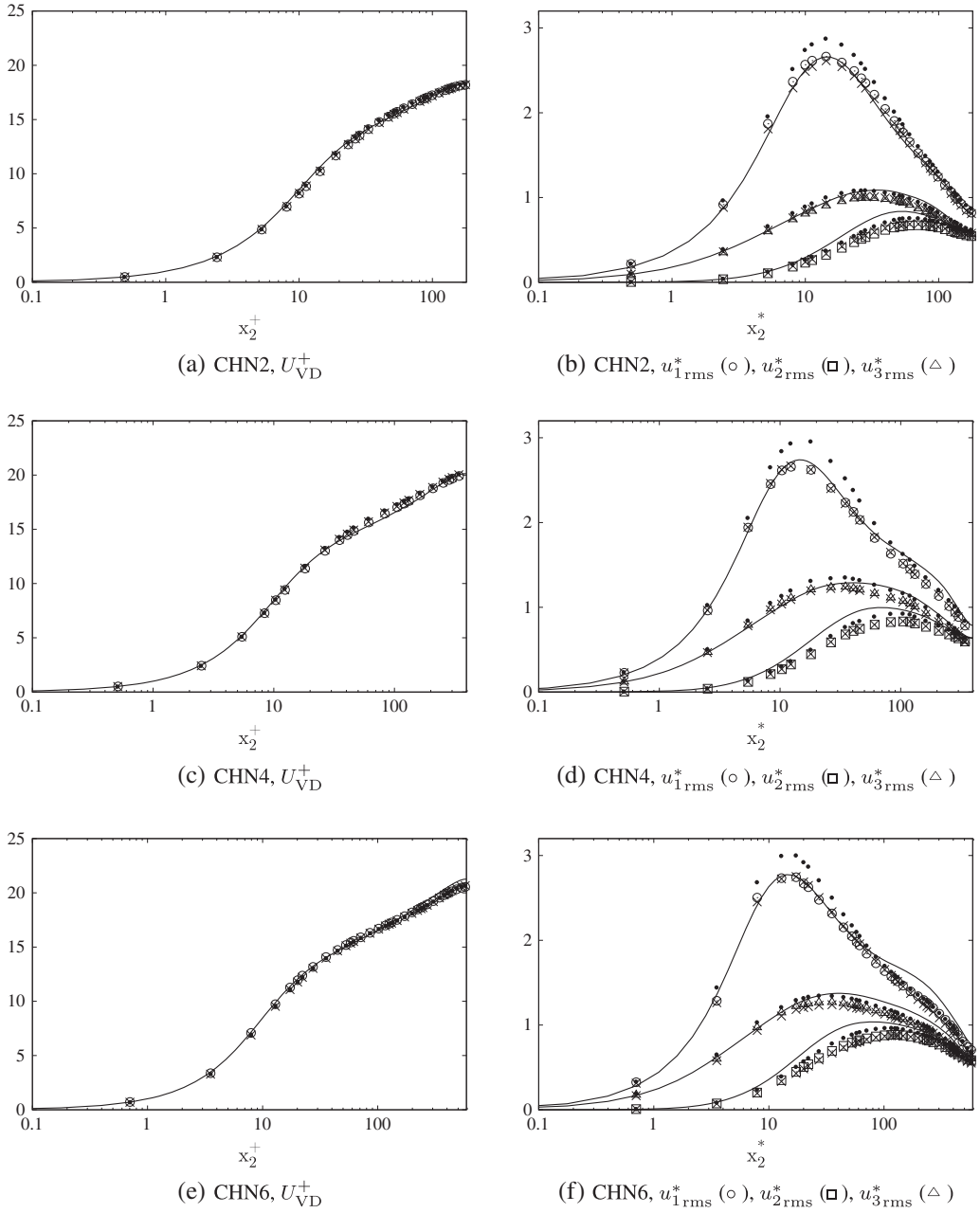

(a) CHN2, U^+_{VD}

(b) CHN2, $u^*_{1\mathrm{rms}}$ (○), $u^*_{2\mathrm{rms}}$ (□), $u^*_{3\mathrm{rms}}$ (△)

(c) CHN4, U^+_{VD}

(d) CHN4, $u^*_{1\mathrm{rms}}$ (○), $u^*_{2\mathrm{rms}}$ (□), $u^*_{3\mathrm{rms}}$ (△)

(e) CHN6, U^+_{VD}

(f) CHN6, $u^*_{1\mathrm{rms}}$ (○), $u^*_{2\mathrm{rms}}$ (□), $u^*_{3\mathrm{rms}}$ (△)

Figure 16. Resolved mean velocity profile (a, c, e) and root mean square of velocity fluctuations (b, d, f) for the cases CHN2, CHN4, and CHN6, with WSM model and the first type of discrete filter (CD1): open symbols, LES on randomly perturbed grid; ×, LES on Cartesian grid; solid circles, implicit LES on randomly perturbed grid; solid lines, DNS data [63].

4. SUMMARY AND CONCLUSIONS

A structural LES model based on the scale similarity hypothesis and the relevant numerical infrastructure has been developed within the high-order unstructured FR framework and, more specifically, for the SD subset. The implementation of such an SGS model, in particular, involved the development of discrete filter operators that are suitable for the standard elements used in these kind of numerical schemes.

DOI: 10.1002/fld

Given the key role played by the discrete filter operators when using similarity mixed models for LES, two sets of constrained filters have been developed to ensure an almost uniform cutoff frequency within the element and a good numerical behavior. One of these sets of filters features strict positivity but is only applicable to standard elements with a specific distribution of solution points, whereas the other set can be applied to arbitrarily distributed points; hence, together, the two sets of discrete filters represent a complete set of discrete operators to be used with discontinuous finite-element-type discretizations. Both sets of discrete filters are completely local inside the standard element; therefore, they are relatively easy to implement and do not involve any additional complication for the parallelism of the numerical solver.

The proposed implementation has been validated on the turbulent channel flow at three different Reynolds numbers, for different orders of accuracy and with both structured and unstructured computational grids. All the results are in very good agreement with available DNS data. Compared with implicit LES computations of the same configurations, the adopted scale similarity WSM model leads to a slight improvement in the first-order statistical moments of the resolved velocity field, while enabling a more accurate reproduction of the Reynolds stresses. Therefore, the use of an SGS model, such as the WSM used in this work, is necessary in applications where an accurate representation of turbulence intensities is crucial, such as for instance those involving turbulent mixing.

The constrained discrete filters of arbitrary order proved to be numerically stable at any order (up to $N = 7$ in other tests not included here) and allow a relatively straightforward implementation into a broad range of high-order discontinuous finite element methods, such as the FR schemes or the SD scheme used in the present work, of any SGS model relying upon the use of explicit filtering or dynamic procedures [72, 73]. Work is currently under way to test the method for a variety of more complex configurations, such as the flow behind square or circular cylinders, or an impinging jet on a wall. Moreover, it is anticipated that further development of wall modeling procedures in conjunction with the unstructured nature of the high-order FR scheme will allow relatively affordable high-fidelity LES computations in a wide range of applications, including hitherto intractable problems of fundamental flow physics and complex geometries of practical engineering interest.

ACKNOWLEDGEMENTS

The authors would like to thank Dr. J. Bodart, S.T. Bose, Prof. C. Liang, and Dr. R. Rossi for stimulating and fruitful discussions. Financial support under NSF grant no. 0915006 monitored by Dr. Leland Jameson and AFOSR grant no. FA 9550-07-1-0195 from the Computational Math Program under the direction of Dr. Fariba Fahroo are gratefully acknowledged.

NOMENCLATURE

β_i^s	normalized position of the ith solution point with respect to the sth solution points
Δt	computational time step
Δ	grid cutoff length scale in computational space
δ	channel half-width
Δ_k^+	equivalent grid spacing (in wall units) in the kth direction
Δ_c	cutoff length scale of the explicit filter
Δ_g	grid cutoff length scale in physical space
δ_{ij}	Kronecker's delta
γ	specific heat ratio ($\gamma = c_\mathrm{p}/c_\mathrm{v}$)
κ	thermal diffusivity
μ	dynamic viscosity
ν	kinematic viscosity
ϖ	macro-pressure [33, 43, 44]
ρ	density
τ_w	mean shear stress at the wall
τ_{ij}	SGS tensor

DOI: 10.1002/fld

ϑ	macro-temperature [33, 43, 44]
ξ_k	kth component of the position vector in computational space
A_{ij}	deviatoric part of the deformation tensor
c_f	friction coefficient
c_p	specific heat capacity at constant pressure
c_v	specific heat capacity at constant volume
C_w	WALE model constant
$\boldsymbol{D}^k$	kth component of the viscous flux vector
e_I	internal energy
$\boldsymbol{\mathcal{F}}^k$	transformed kth component of the flux vector
$\boldsymbol{F_I}^k$	kth component of the inviscid flux vector
$\boldsymbol{F}^k$	kth component of the flux vector
F_w	instantaneous resultant shear at the wall
g_{ij}	velocity gradient tensor
h_i	Lagrange basis for the ith solution point
$\boldsymbol{J}$	Jacobian of the transformation between physical and computational spaces
j	imaginary constant
k	wavenumber
ℓ_τ	viscous length ($\ell_\tau = \nu/u_\tau$)
l_i	Lagrange basis for the ith flux point
$\dot{m}$	mass flow rate
M_k	kth shape function
N	number of solution points in the element
N_p	number of points used to define the physical element
Pr	Prandtl number
p	pressure
P_n	Legendre polynomial of order n
q_k	SGS heat flux
Re	Reynolds number
Re_τ	Reynolds number based on the friction velocity and channel half-width
Re_m	Reynolds number based on the bulk velocity and channel width
R	gas constant
$\boldsymbol{\mathcal{S}}$	transformed source term vector
$\boldsymbol{S}$	source term vector
s_{ij}^d	traceless symmetric part of the square of the velocity gradient tensor
s_k	kth component of the source term vector
T	temperature
t	time
$\boldsymbol{\mathcal{U}}$	transformed vector of conservative variables
$\boldsymbol{U}$	vector of conservative variables
U_VD^+	Van-Driest-corrected mean streamwise velocity
u_b	bulk velocity
u_τ	friction velocity $\left(u_\tau^2 = \tau_\mathrm{w}/\rho\right)$
u_k	kth component of the velocity vector
w_i^s	ith weight coefficient for the sth filter operator
x_k	kth component of the position vector

REFERENCES

1. Lele SK. Compact finite difference schemes with spectral-like resolution. *Journal of Computational Physics* 1992; **103**(1):16–42.
2. Nagarajan S, Lele SK, Ferziger JH. A robust high-order compact method for large eddy simulation. *Journal of Computational Physics* 2003; **191**(2):392–419.

DOI: 10.1002/fld

3. Visbal MR, Gaitonde DV. On the use of higher-order finite-difference schemes on curvilinear and deforming meshes. *Journal of Computational Physics* 2002; **181**(1):155–185.
4. Visbal MR, Rizzetta DP. Large-eddy simulation on curvilinear grids using compact differencing and filtering schemes. *Journal of Fluids Engineering* 2002; **124**(4):836–847.
5. Galbraith MC, Visbal MR. Implicit large eddy simulation of low Reynolds number flow past the SD7003 airfoil. *46th AIAA Aerospace Sciences Meeting and Exhibit*, Reno, NV, January 7–10, 2008; 1–17. AIAA Paper 2008-225.
6. Hesthaven JS, Warburton T. *Nodal Discontinuous Galerkin Methods: Algorithms, Analysis, and Applications*. Springer Science+ Business Media, LLC: Heidelberg, 2008. ISBN 978-0-387-72065-4.
7. Karniadakis G, Sherwin SJ. *Spectral/Hp Element Methods for CFD*. Oxford University Press: New York, 1999.
8. Kopriva DA, Kolias JH. A conservative staggered-grid Chebyshev multidomain method for compressible flows. *Journal of Computational Physics* 1996; **125**(1):244–261.
9. Huynh HT. A flux reconstruction approach to high-order schemes including discontinuous Galerkin methods. *18th AIAA Computational Fluid Dynamics Conference*, Miami, FL, June 25–28, 2007; 1–42. AIAA Paper 2007-4079.
10. Huynh HT. A reconstruction approach to high-order schemes including discontinuous Galerkin for diffusion. *47th AIAA Aerospace Sciences Meeting*, Orlando, FL, January 5–8, 2009; 1–34. AIAA Paper 2009-403.
11. Liu Y, Vinokur M, Wang ZJ. Spectral difference method for unstructured grids I: basic formulation. *Journal of Computational Physics* 2006; **216**(2):780–801.
12. May G, Jameson A. A spectral difference method for the Euler and Navier–Stokes equations on unstructured meshes. *44th AIAA Aerospace Sciences Meeting*, Reno, NV, January 9–12, 2006; 1–18. AIAA Paper 2006-304.
13. Sun Y, Wang ZJ, Liu Y. High-order multidomain spectral difference method for the Navier–Stokes equations on unstructured hexahedral grids. *Communications in Computational Physics* 2007; **2**(2):310–333.
14. Wang ZJ, Liu Y, May G, Jameson A. Spectral difference method for unstructured grids II: extension to the Euler equations. *Journal of Scientific Computing* 2007; **32**(1):45–71.
15. Liang C, Jameson A, Wang ZJ. Spectral difference method for compressible flow on unstructured grids with mixed elements. *Journal of Computational Physics* 2009; **228**(8):2847–2858.
16. Jameson A. A proof of the stability of the spectral difference method for all orders of accuracy. *Journal of Scientific Computing* 2010; **45**(1):348–358.
17. Vincent PE, Castonguay P, Jameson A. A new class of high-order energy stable flux reconstruction schemes. *Journal of Scientific Computing* 2010; **47**(1):1–23.
18. Vincent PE, Castonguay P, Jameson A. Insights from von Neumann analysis of high-order flux reconstruction schemes. *Journal of Computational Physics* 2011; **230**(22):8134–8154.
19. Castonguay P, Vincent PE, Jameson A. A new class of high-order energy stable flux reconstruction schemes for triangular elements. *Journal of Scientific Computing* 2012; **51**(1):224–256.
20. Williams D, Castonguay P, Vincent PE, Jameson A. An extension of energy stable flux reconstruction to unsteady, non-linear, viscous problems on mixed grids. *20th AIAA Computational Fluid Dynamics Conference*, Honolulu, Hawaii, June 27–30, 2011; 1–37. AIAA Paper 2011-3405.
21. Ou K, Vincent PE, Jameson A. High-order methods for diffusion equation with energy stable flux reconstruction scheme. *49th AIAA Aerospace Sciences Meeting Including the New Horizons Forum and Aerospace Exposition*, Orlando, FL, January 4–7, 2011; 1–19. AIAA Paper 2011-46.
22. Premasuthan S, Liang C, Jameson A. A spectral difference method for viscous compressible flows with shocks. *19th AIAA Computational Fluid Dynamics*, San Antonio, TX, June 22–25, 2009; 1–16. AIAA Paper 2009-3785.
23. Liang C, Premasuthan S, Jameson A, Wang ZJ. Large eddy simulation of compressible turbulent channel flow with spectral difference method. *47th AIAA Aerospace Sciences Meeting Including the New Horizons Forum and Aerospace Exposition*, Orlando, FL, January 5–8, 2009; 1–15. AIAA Paper 2009-402.
24. Liang C, Premasuthan S, Jameson A. High-order accurate simulation of low-Mach laminar flow past two side-by-side cylinders using spectral difference method. *Computers & Structures* 2009; **87**(11–12):812–827.
25. Mohammad AH, Wang ZJ, Liang C. Large eddy simulation of flow over a cylinder using high-order spectral difference method. *Advances in Applied Mathematics and Mechanics* 2010; **2**(4):451–466.
26. Ou K, Liang C, Premasuthan S, Jameson A. High-order spectral difference simulation of laminar compressible flow over two counter-rotating cylinders. *27th AIAA Applied Aerodynamics Conference*, San Antonio, TX, June 22–25, 2009; 1–22. AIAA Paper 2009-3956.
27. Castonguay P, Liang C, Jameson A. Simulation of transitional flow over airfoils using the spectral difference method. *AIAA Paper 2010-4626*, 2010.
28. Parsani M, Ghorbaniasl G, Lacor C, Turkel E. An implicit high-order spectral difference approach for large eddy simulation. *Journal of Computational Physics* 2010; **229**(14):5373–5393.
29. Nicoud F, Ducros F. Subgrid-scale stress modelling based on the square of the velocity gradient tensor. *Flow, Turbulence and Combustion* 1999; **62**(3):183–200.
30. Parsani M, Ghorbaniasl G, Lacor C. Validation and application of an high-order spectral difference method for flow induced noise simulation. *Journal of Computational Acoustics* 2011; **19**(3):241–268.
31. Bardina J, Ferziger JH, Reynolds WC. Improved subgrid-scale models for large-eddy simulation. *13th Fluid and Plasma Dynamics Conference*, Snowmass, CO, July 14–16, 1980; 1–10. AIAA Paper 1980-1357.
32. Bardina J, Ferziger JH, Reynolds WC. Improved turbulence models based on LES of homogeneous incompressible turbulent flows. *Report TF-19*, Thermosciences Division, Dept. of Mechanical Engineering, Stanford University, 1984.

DOI: 10.1002/fld

33. Lodato G, Vervisch L, Domingo P. A compressible wall-adapting similarity mixed model for large-eddy simulation of the impinging round jet. *Physics of Fluids* 2009; **21**(3):035102.
34. Liu S, Meneveau C, Katz J. On the properties of similarity subgrid-scale models as deduced from measurements in a turbulent jet. *Journal of Fluid Mechanics* 1994; **275**:83–119.
35. Meneveau C, Katz J. Scale-invariance and turbulence models for large-eddy simulation. *Annual Review of Fluid Mechanics* 2000; **32**(1):1–32.
36. Blackburn HM, Schmidt S. Spectral element filtering techniques for large eddy simulation with dynamic estimation. *Journal of Computational Physics* 2003; **186**(2):610–629.
37. Sengupta K, Jacobs GB, Mashayek F. Large-eddy simulation of compressible flows using a spectral multidomain method. *International Journal for Numerical Methods in Fluids* 2009; **61**(3):311–340.
38. Jameson A, Vincent PE, Castonguay P. On the non-linear stability of flux reconstruction schemes. *Journal of Scientific Computing* 2012; **50**(2):434–445.
39. Roe PL. Approximate Riemann solvers, parameter vectors, and difference schemes. *Journal of Computational Physics* 1981; **43**:357–372.
40. Harten A. High resolution schemes for hyperbolic conservation laws. *Journal of Computational Physics* 1983; **49**(3):357–393.
41. Jiang GS, Shu CW. Efficient implementation of weighted ENO schemes. *Journal of Computational Physics* 1996; **126**:202–228.
42. Gottlieb S, Shu CW. Total variation diminishing Runge–Kutta schemes. *Mathematics of Computation* 1998; **67**(221):73–85.
43. Ducros F, Comte P, Lesieur M. Large-eddy simulation of a spatially growing boundary layer over an adiabatic flat plate at low Mach number. *International Journal of Heat and Fluid Flow* 1995; **16**(5):341–348.
44. Lesieur M, Métais O, Comte P. *Large-Eddy Simulations of Turbulence*. Cambridge University Press: Cambridge, MA, 2005. ISBN 0-521-78124-8.
45. Monin AS, Yaglom AM. *Statistical Fluid Mechanics: Mechanics of Turbulence*, Vol. I. Dover Publications, Inc.: Mineola, NY, 1971. ISBN 0-486-45883-0.
46. Schlichting H, Gersten K. *Boundary-Layer Theory*, 8th edition. Springer-Verlag: Berlin, 2000. ISBN 3-540-66270-7.
47. Sagaut P. *Large Eddy Simulation for Incompressible Flows: An Introduction*, 2nd edition. Springer-Verlag: Berlin, 2001. ISBN 3-540-43753-3.
48. Akhavan R, Ansari A, Kang S, Mangiavacchi N. Subgrid-scale interactions in a numerically simulated planar turbulent jet and implications for modeling. *Journal of Fluid Mechanics* 2000; **408**:83–120.
49. Salvetti MV, Banerjee S. *A priori* tests of a new dynamic subgrid-scale model for finite-difference large-eddy simulations. *Physics of Fluids* 1995; **7**(11):2831–2847.
50. Anderson R, Meneveau C. Effects of the similarity model in finite-difference LES of isotropic turbulence using a Lagrangian dynamic mixed model. *Flow, Turbulence and Combustion* 1999; **62**(3):201–225.
51. Zang TA, Dahlburg RB, Dahlburg JP. Direct and large-eddy simulations of three-dimensional compressible Navier–Stokes turbulence. *Physics of Fluids A: Fluid Dynamics* 1992; **4**(1):127–140.
52. Zang Y, Street RL, Koseff JR. A dynamic mixed subgrid-scale model and its application to turbulent recirculating flows. *Physics of Fluids A: Fluid Dynamics* 1993; **5**(12):3186–3196.
53. Erlebacher G, Hussaini MY, Speziale CG, Zang TA. Toward the large-eddy simulation of compressible turbulent flows. *Journal of Fluid Mechanics* 1992; **238**:155–185.
54. Speziale CG. Galilean invariance of subgrid-scale stress models in the large-eddy simulation of turbulence. *Journal of Fluid Mechanics* 1985; **156**:55–62.
55. Speziale CG, Erlebacher G, Zang TA, Hussaini MY. The subgrid-scale modeling of compressible turbulence. *Physics of Fluids* 1988; **31**(4):940–942.
56. Temmerman L, Leschziner MA, Mellen CP, Fröhlich J. Investigation of wall-function approximations and subgrid-scale models in large eddy simulation of separated flow in a channel with streamwise periodic constrictions. *International Journal of Heat and Fluid Flow* 2003; **24**(2):157–180.
57. Lodato G. Conditions aux Limites Tridimensionnelles pour la Simulation Directe et aux Grandes Echelles des Ecoulements Turbulents. Modélisation de Sous-Maille pour la Turbulence en Région de Proche Paroi. *PhD Thesis*, INSA de Rouen, UMR-CNRS-6614-CORIA, December 2008. (Available from: http://www.coria.fr/spip.php?article552) [accessed on March 2009].
58. Vasilyev OV, Lund TS, Moin P. A general class of commutative filters for LES in complex geometries. *Journal of Computational Physics* 1998; **146**(1):82–104.
59. Berland J, Bogey C, Marsden O, Bailly C. High-order, low dispersive and low dissipative explicit schemes for multiple-scale and boundary problems. *Journal of Computational Physics* 2007; **224**(2):637–662.
60. Sagaut P, Grohens R. Discrete filters for large eddy simulation. *International Journal for Numerical Methods in Fluids* 1999; **31**(8):1195–1220.
61. Lund TS. On the use of discrete filters for large eddy simulation. In *Annual Research Briefs*, Moin P, Reynolds WC (eds). Center for Turbulence Research, Stanford University: Stanford, 1997; 83–95.
62. Vreman AW. The adjoint filter operator in large-eddy simulation of turbulent flow. *Physics of Fluids* 2004; **16**(6):2012–2022.
63. Moser RD, Kim J, Mansour NN. Direct numerical simulation of turbulent channel flow up to $\mathrm{Re}_\tau = 590$. *Physics of Fluids* 1999; **11**(4):943–945.

DOI: 10.1002/fld

64. Van Driest ER. Turbulent boundary layer in compressible fluids. *Journal of Spacecraft and Rockets* 2003; **40**(6):1012–1028. Reprint of the original paper in *J. Aeronaut. Sci.* (1951), vol. 18(3):145–160.
65. Coleman GN, Kim J, Moser RD. A numerical study of turbulent supersonic isothermal-wall channel flow. *Journal of Fluid Mechanics* 1995; **305**:159–183.
66. Huang PG, Coleman GN, Bradshaw P. Compressible turbulent channel flows: DNS results and modelling. *Journal of Fluid Mechanics* 1995; **305**:185–218.
67. Foysi H, Sarkar S, Friedrich R. Compressibility effects and turbulence scalings in supersonic channel flow. *Journal of Fluid Mechanics* 2004; **509**(1):207–216.
68. Lenormand E, Sagaut P, Ta Phuoc L. Large eddy simulation of subsonic and supersonic channel flow at moderate Reynolds number. *International Journal for Numerical Methods in Fluids* 2000; **32**:369–406.
69. Andersson P, Brandt L, Bottaro A, Henningson DS. On the breakdown of boundary layer streaks. *Journal of Fluid Mechanics* 2001; **428**(1):29–60.
70. Rossi R. Direct numerical simulation of scalar transport using unstructured finite-volume schemes. *Journal of Computational Physics* 2009; **228**(5):1639–1657.
71. Geurts BJ, Fröhlich J. A framework for predicting accuracy limitations in large-eddy simulation. *Physics of Fluids* 2002; **14**(6):L41–L44.
72. Germano M, Piomelli U, Moin P, Cabot WH. A dynamic subgrid-scale eddy viscosity model. *Physics of Fluids A: Fluid Dynamics* 1991; **3**(7):1760–1765.
73. Moin P, Squires K, Cabot W, Lee S. A dynamic subgrid-scale model for compressible turbulence and scalar transport. *Physics of Fluids A: Fluid Dynamics* 1991; **3**(11):2746–2757.

DOI: 10.1002/fld